

The Meridional Oceanic Transports of Heat and Nutrients in the South Atlantic

JÜRGEN HOLFORT* AND GEROLD SIEDLER[†]

Institut für Meereskunde an der Universität Kiel, Kiel, Germany

(Manuscript received 28 December 1998, in final form 3 February 2000)

ABSTRACT

Meridional transports of mass, heat, nutrients, and carbon across coast-to-coast WOCE and pre-WOCE sections between 11°S and 45°S in the South Atlantic are calculated using an inverse model. Usually salt preservation is used as a condition in the inverse model, and only in the case of heat transport the condition of zero total mass transport is taken instead. Other constraints include silica conservation, prescribed southward fluxes of salt and phosphate, and transports in the southward Brazil Current and in the northward Antarctic Bottom Water flow obtained from WOCE moored current meter arrays. The constraints set the underdetermined system of linear equations of the inverse model whose solutions depend on weights, scales, and matrix ranks. The discussion emphasizes the sensitivity of the fluxes to changes in the model input. The transports given in the following are obtained as the means of “reasonable” solutions at 30°S. The error numbers in parentheses include uncertainties due to wind stress and temporal variability, the numbers without parentheses do not contain these terms: 0.53 ± 0.03 (0.09) Tg s^{-1} mass to the south, 0.29 ± 0.05 (0.24) PW heat to the north, 15 ± 120 (500) kmol s^{-1} oxygen to the south, 121 ± 22 (75) kmol s^{-1} nitrate to the south, 64 ± 110 (300) silica to the north, and 1997 ± 215 (600) kmol s^{-1} dissolved inorganic carbon to the south. The above errors in transports are obviously dominated by uncertainties in wind stress and temporal variability. The divergence in meridional heat and mass transport is consistent with integral surface flux changes between corresponding zonal bands. The mass compensation of southward flowing North Atlantic Deep Water occurs to a greater extent in the warm surface waters than in the Antarctic Intermediate Water below. If one follows the arguments of earlier authors on the relation between meridional fluxes and the significance of the two possible pathways for the global thermohaline circulation, the warm water path south of Africa seems to be somewhat more important than the cold water path through Drake Passage.

1. Introduction

The South Atlantic serves as the passage between the key water mass formation regions of the global ocean. Cold North Atlantic Deep Water, having been formed by convection and mixing in the northern North Atlantic, flows southward at depth, and the compensating return flow at intermediate and shallow levels transports warmer water from the Pacific and Indian Oceans to the North Atlantic. Also cold subpolar and polar water masses, having been formed mostly in the Weddell Sea, arrive from the south and contribute to the meridional transports. While the zonally averaged global meridional heat flux in the ocean is poleward and nearly sym-

metric to the equator, the heat flux in the South Atlantic has a different pattern. The excessive heat loss of the North Atlantic to the atmosphere has to be compensated by heat provided from the other oceans, and this results in a northward mean meridional heat flux throughout the Atlantic.

The present study in the South Atlantic is mainly based on observations during the World Ocean Circulation Experiment (WOCE). The main goal of WOCE is to determine the large-scale oceanic circulation as a basis for developing and testing ocean circulation models and coupled climate change models. Providing reliable estimates of meridional heat transports in the different oceans is a key requirement in this context, and the South Atlantic is particularly important because of its passage function in the global thermohaline circulation. As has been discussed by Gordon (1986) and Rintoul (1991), an estimate of the meridional heat flux between the circumpolar region and the subtropical South Atlantic can provide a critical number for the determination of the branches contributing to the global circulation, either the westward “warm water path” south of Africa or the eastward “cold water path” through Drake Passage.

* Current affiliation: Institut für Meereskunde an der Universität Hamburg, Hamburg, Germany.

[†] Current affiliation: Instituto Canario de Ciencias Marinas, Telde, Grand Canary, Spain.

Corresponding author address: Dr. Jürgen Holfort, Institut für Meereskunde, Universität Hamburg, Troplowitzstraße 7, D-22529 Hamburg, Germany.
E-mail: holfort@ifm.uni-hamburg.de

TABLE 1. Sections used in this study.

Cruise	Year	Position	Reference
OCEANUS 133	1983	11°S and 23°S, 30°W	Warren and Speer (1991)
WOCE A8	1994	11°S	Zenk and Müller (1995)
WOCE A9	1991	19°S, 15°W	Siedler and Zenk (1992)
WOCE A10	1993	30°S	Siedler et al. (1993)
SAVE leg 3	1988	25°SW, 0°W	STS/ODF (1992a)
SAVE leg 4	1988	25°SE	STS/ODF (1992b)
SAVE leg 6	1988	25°W	STS/ODF (1992c)
WOCE A11	1993	45°–30°S	Saunders and King (1995)

Here we present results on heat and also on nutrient fluxes in the South Atlantic that were obtained from selected zonal WOCE and pre-WOCE hydrographic sections and also from direct current observations performed during WOCE in the western boundary current region. An inverse model is used for determining the heat transports between 11°S and 45°S. A major difficulty in obtaining a reliable heat flux estimate is the determination of a sufficiently accurate absolute meridional velocity field in the ocean. A major part of the following presentation is therefore devoted to the method of calculating the meridional velocity distribution.

After a short description of the dataset used, the method of flux determination using geostrophic calculations combined with wind stress data will be presented. This will be followed by a presentation of the constraints used in the inverse calculations. In selecting the constraints emphasis will be given to the direct current measurements in the western boundary region including the Brazil Current, the Intermediate and North Atlantic Deep Water flow, and the Antarctic Bottom Water flow into the Brazil Basin. After a discussion of the influence of weighting, scaling, and matrix rank on the inverse calculations and the associated residuals, we will conclude with the resulting meridional fluxes and a dis-

cussion of the results in the context of the global thermohaline circulation.

2. Hydrographic data and direct current measurements

Hydrographic datasets with high-quality CTD observations were selected from cruises in the South Atlantic between 11°S and 45°S during the period 1983–1993. Table 1 contains an overview of the cruises, and the positions of the stations used are shown in Fig. 1. All data are from the austral summer (Jan–Mar). It is noted that the WOCE section A11 was only used in a subset of the inverse analysis.

WOCE data are submitted to an international quality check. At the time this analysis was performed only sections A9 and A11 had already passed the final international evaluation, and are considered accurate to 0.002°C in temperature, 0.002 in salinity, and 3 dbar in pressure. The more recent WOCE data will be of similar quality.

Some parameter values were missing on certain stations, for example, phosphate concentration (PO_4) was not obtained on section A8 and total dissolved inorganic carbon (DIC) was not measured on OCEANUS 133. In

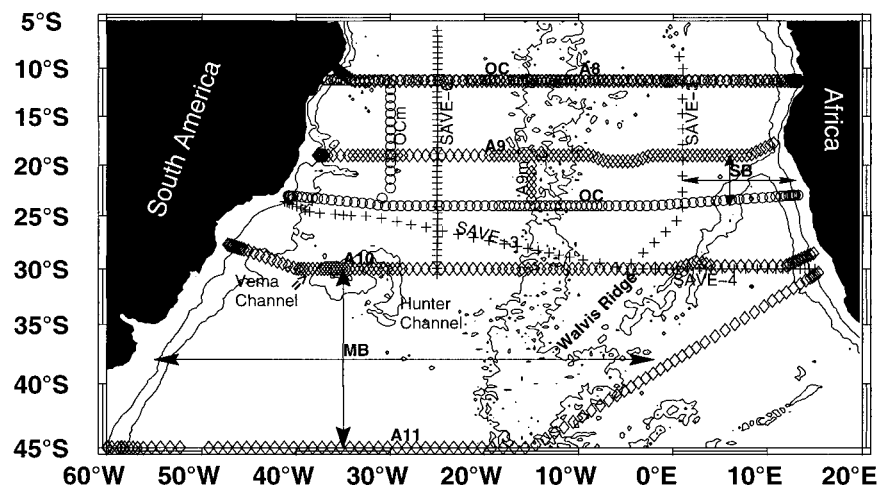


FIG. 1. Positions of the hydrographic sections (WOCE sections are labeled A8, A9, A10, and A11, OCEANUS are labeled OC, and SAVE sections are labeled SAVE-3, SAVE-4 and SAVE-6) used in the present study. The isobaths at 1000 and 3500 m are shown. Also shown is a main box (MB) and a secondary box (SB) of the inverse model.

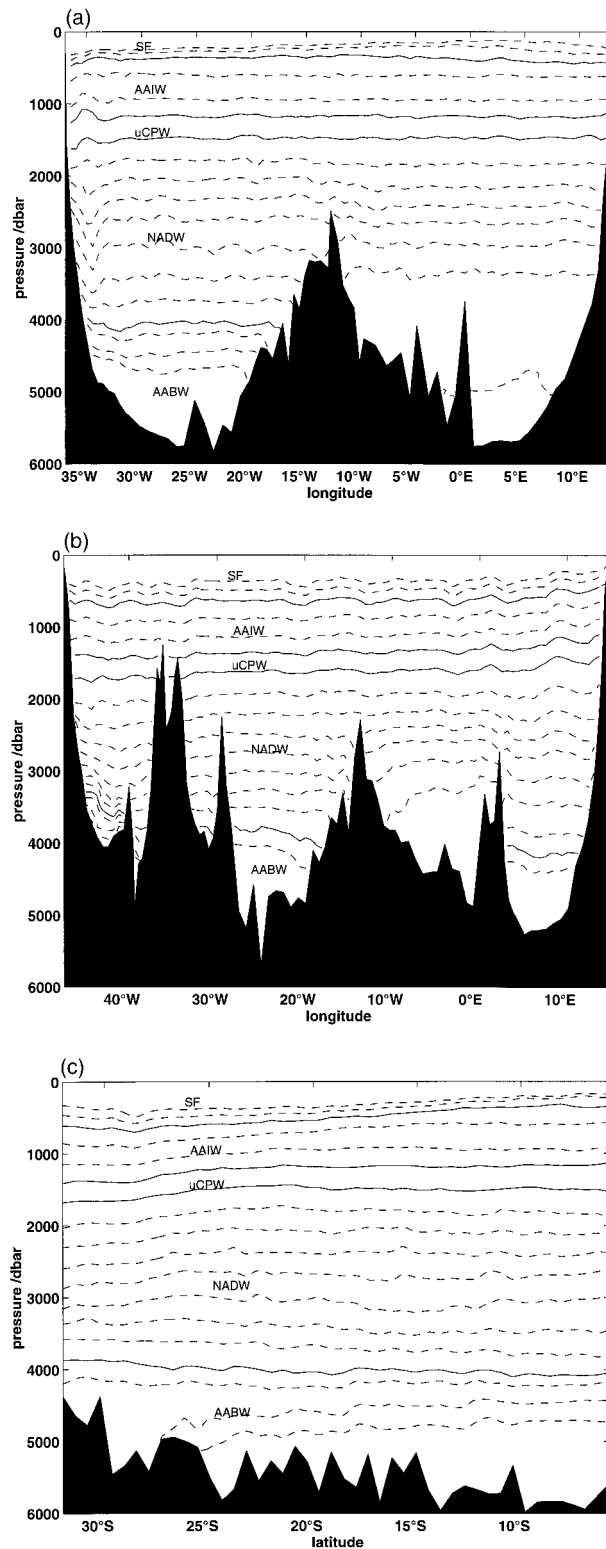


FIG. 2. Sections of density interfaces at (a) WOCE A8 (11°S), (b) WOCE A10 (30°S), and (c) SAVE-6 (30°W). For definitions see Table 2. The density interfaces separating different water masses are shown solid. The water masses are surface water (SF), Antarctic Intermediate Water (AAIW), upper Circumpolar Water (uCPW), North Atlantic Deep Water (NADW), and Antarctic Bottom Water (AABW).

TABLE 2. Mass transport (at 30°S in Tg s^{-1}) and upper boundaries of water masses given by the sea surface and by isopycnal surfaces. The terms σ_0 , σ_1 , σ_2 , σ_3 , and σ_4 represent the densities of the water if brought adiabatically to 0, 1000, 2000, 3000, or 4000 dbar, respectively.

Water mass	T_{mass}	This study	Roemmich (1983)	Macdonald (1993)
Surface	6.0	Surface	Surface	Surface
	2.8	$\sigma_0 = 26.60$	$\sigma_0 = 26.20$	$\sigma_0 = 26.60$
	1.6	$\sigma_0 = 26.80$		$\sigma_0 = 26.80$
AAIW	1.9	$\sigma_0 = 27.00$	$\sigma_0 = 26.80$	$\sigma_0 = 27.00$
	2.1	$\sigma_0 = 27.20$	$\sigma_0 = 27.00$	$\sigma_0 = 27.02$
	-0.2	$\sigma_1 = 32.00$		$\sigma_1 = 32.00$
uCPW	-1.9	$\sigma_1 = 32.16$	$\sigma_0 = 27.40$	$\sigma_1 = 32.16$
				$\sigma_2 = 36.73$
NADW	-3.5	$\sigma_2 = 36.82$	$\sigma_2 = 36.90$	$\sigma_2 = 36.80$
	-3.3	$\sigma_2 = 36.92$	$\sigma_2 = 37.07$	$\sigma_2 = 36.92$
	-2.3	$\sigma_2 = 36.97$		$\sigma_2 = 36.97$
	-2.3	$\sigma_2 = 37.00$		$\sigma_2 = 37.00$
	-1.9	$\sigma_2 = 37.02$		
	-3.4	$\sigma_2 = 37.04$		$\sigma_2 = 37.04$
	-2.7	$\sigma_3 = 41.50$		
	-0.2	$\sigma_3 = 41.53$		$\sigma_3 = 41.54$
AABW	0.7	$\sigma_4 = 45.93$	$\sigma_4 = 45.92$	$\sigma_4 = 45.93$
	2.0	$\sigma_4 = 45.96$		$\sigma_4 = 45.96$
	1.0	$\sigma_4 = 46.00$		$\sigma_4 = 46.00$
	3.1	$\sigma_4 = 46.02$		$\sigma_4 = 46.02$

order to obtain a complete dataset at each station, bottle data from a $2^\circ \times 2^\circ$ square (or larger if data coverage was inadequate) around the station were used to interpolate missing parameter values, using multiple linear regression (see Holfort et al. 1998). The errors associated with this mapping scheme are about twice the respective measurement uncertainties.

In the later analysis water mass layers between certain isopycnal surfaces will be considered. We first present selected sections for these isopycnals in Fig. 2. From bottom to top the layers represent the Antarctic Bottom Water (AABW), the North Atlantic Deep Water (NADW), upper Circumpolar Water (UCPW), the Antarctic Intermediate Water (AAIW), and the surface water (SF). The densities at the water mass boundaries are given in Table 2 in comparison with the corresponding choices of Macdonald (1993) and Roemmich (1983). A description of the water masses in the South Atlantic based also on other parameters and corresponding sections can be found in Reid (1989) and Siedler et al. (1996).

The second type of data used in this study results from direct current measurements made at the Rio Grande Ridge between 28° and 31°S , during the period from January 1991 to November 1992. These observations were part of a joint project of the Institut für Meereskunde at Kiel (IfM) and Woods Hole Oceanographic Institute (Tarbell et al. 1994; Hogg et al. 1999). We here use data from three IfM moorings in the Brazil Current region and from three IfM moorings in the Vema Channel (Fig. 3, Table 3).

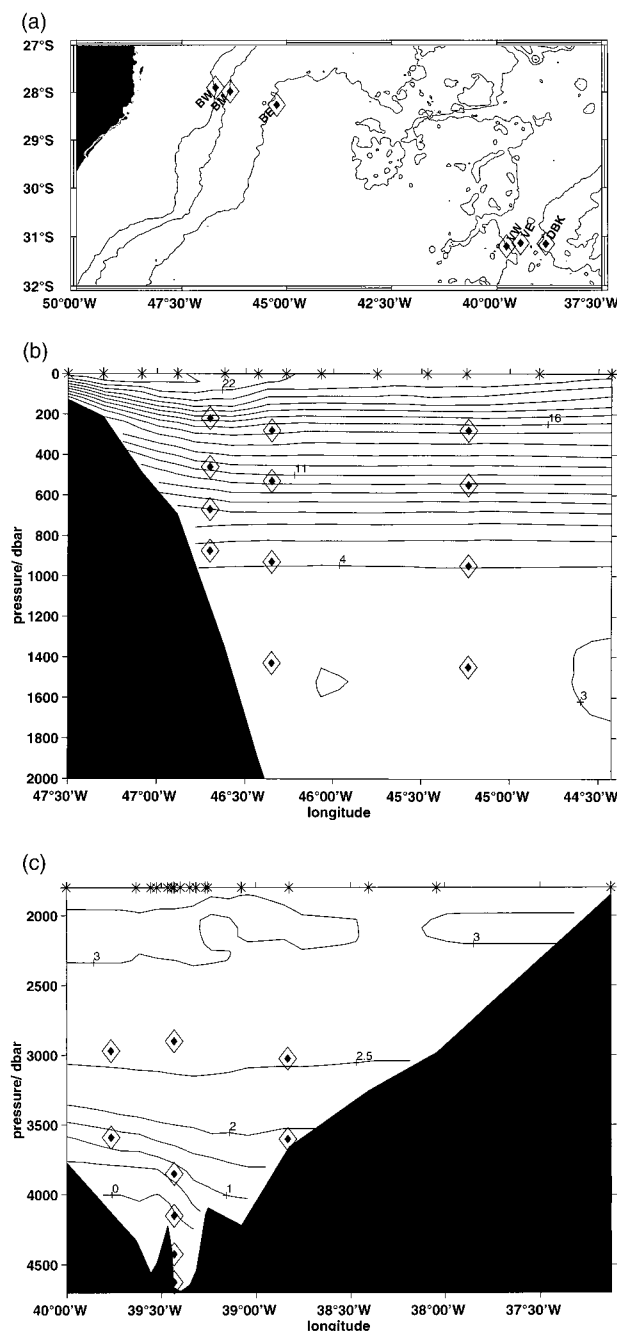


FIG. 3. Map with the mooring positions (a) and vertical sections of potential temperature including the locations of the current meters in the Brazil Current region (b) and at the Vema Channel (c), with the data for the contours taken from *Meteor* Cruise 22/3 (Siedler et al. 1993). Asterisks at the surface mark the positions of the CTD profiles used. Isobaths in (a) at 1000-m intervals.

The data were low-pass filtered with a 36-h cutoff and then averaged to daily values. The pressure and temperature data from the Brazil Current moorings on the continental slope and near the shelf edge (see Table 4) indicate that moorings BE and BM tilted considerably at certain times, and the respective velocities from cur-

TABLE 3. Mooring positions and deployment periods.

Mooring					
Name	Num-ber	Latitude	Longitude	Launch date	Recovery date
BW	333	27°54'S	46°42'W	01.01.1991	27.11.1992
BM	334	27°59'S	46°21'W	01.01.1991	27.11.1992
BE	335	28°16'S	45°14'W	03.01.1991	26.11.1992
VW	336	31°12'S	39°46'W	09.01.1991	06.12.1992
VE	338	31°08'S	39°26'W	11.01.1991	06.12.1992
DBK	343	31°09'S	38°50'W	12.01.1991	07.12.1992

rent meters cannot be considered to be representative for a constant depth level. The velocity measurements from the Brazil Current moorings are therefore not used directly. Instead a velocity profile at 50-m intervals is constructed for each mooring using a decomposition into normal modes similar to the method earlier used by Müller and Siedler (1992). In addition to the Aanderaa current meter data, three bins of data from an upward-looking acoustic Doppler current profiler (ADCP) are used at mooring BW, and five bins at mooring BE. The amplitudes of the different modes are calculated from the daily values, and the velocity profile is determined from the first three modes at moorings BW and BE. Only the first two modes are used at BM because no ADCP data are available there.

The obtained vertical velocity profiles from the three moorings at 28°S are used to estimate the transport of the Brazil Current whose vertical extent is assumed to be from the surface to 600 m (Stramma 1989). The Brazil Current is thus defined as the southward boundary current in the upper layer only, not including the flow in the AAIW or NADW. Actually, the AAIW below the near-surface water moves in almost the same direction at this latitude, as has been documented by mooring and deep float data (Boebel et al. 1997). It is noted that the overall southward flow in the boundary region can even reach to the bottom as described by Hogg et al. (1999), who combined direct velocity measurements with dynamic computations. Their Fig. 5a indicates, however, that despite the deep-reaching southward flow, a well-defined core of a near-surface Brazil Current can be recognized, and that the widths of integration chosen here will provide a reasonably good approximation of this part of the southward boundary transport.

In our transport calculation each mean vertical current profile is assumed to be representative for a cross section extending to both sides of the respective mooring. The cross-sectional limits are: the approximate position of the shelf edge in the west, the midpoints between the three moorings, and an eastern boundary corresponding to a symmetric cross section at the eastern mooring. This leads to widths of 70 km, 84 km and 114 km from west to east, respectively. The transports are calculated for a direction of 200°, which is perpendicular to the cross-sectional area chosen and almost parallel to the mean velocity vector (see Table 4). The distribution of

TABLE 4. Minimum and maximum pressure observed by the upper instruments of the Brazil Current moorings BW, BM, and BE; mean speeds and directions; minimum and maximum temperatures; and the assumed cross-sectional width (see text).

Mooring name	Nominal depth (m)	Pressure		Mean speed cm s^{-1}	Mean direction (deg)	Temperature		Width (km)
		Minimum (dbar)	Maximum (dbar)			Minimum ($^{\circ}\text{C}$)	Maximum ($^{\circ}\text{C}$)	
BW	220	215	303	29.85	209	13.19	19.68	70
BW	460	461	539	16.05	212	8.65	12.64	70
BW	670	—	—	6.09	212	5.61	8.00	70
BW	875	—	—	1.95	296	4.11	5.30	70
BM	280	244	813	10.29	214	6.78	18.11	84
BM	530	497	1001	7.87	218	5.17	12.37	84
BM	930	—	—	3.73	218	3.74	5.04	84
BM	1430	—	—	3.20	202	3.13	3.70	84
BM	2137	—	—	1.23	15	3.17	3.83	84
BE	280	243	654	1.79	314	7.01	17.74	114
BE	550	550	953	1.23	288	4.90	12.13	114
BE	950	—	—	1.55	253	3.59	4.81	114
BE	1450	—	—	3.47	247	2.91	3.67	114
BE	2545	—	—	2.55	238	3.03	3.33	114
BE	3208	—	—	4.79	20	0.51	1.99	114

the daily transports is close to Gaussian and the mean value of the transport is 9.7 Sv ($\text{Sv} \equiv 10^6 \text{ m}^3 \text{ s}^{-1}$) or approximately 10 Tg s^{-1} (a mass transport of 1 Tg s^{-1} corresponds to an approximate volume transport of 1 Sv). The extreme values usually occurred when the quality of vertical interpolation was obviously poor. The mean value of the obtained total Brazil Current transport lies in the (rather wide) range of transports inferred by other authors from hydrographic data with an assumed level of no motion (see Fig. 4).

Since the moorings farther to the east in the Vema Channel (see Table 5) did not tilt strongly and because the effect of mooring line inclination on instrument depth is smaller close to the bottom, the bottom water

transport can be calculated directly by using daily averages of the 36-h low-pass filtered data from the three moorings (VW336, VE338, and DBK343) in the Vema Channel region. Each current meter was again assumed to be representative for a certain cross-sectional area. The vertical boundaries of these areas were chosen halfway between the moorings and were symmetric for the moorings in the west and the east. The resulting horizontal width was 32.5 km at VW336 in the west and 57 km at DBK343 in the east. Assuming a moderate change of current velocity at depth near those two moorings, the bottom of the respective cross section can be taken as the mean depth. The highest velocities occur at great depth in the central valley at mooring VE338, and the bottom profile is approximately U-shaped there. Bathymetric charts were used to estimate the effective width of the box around each current meter, with the width changing from 14 km at the deepest current meter at 4625 m to 44 km at 3850 m and above.

As upper boundary for the AABW we considered two choices: 3500 m or the depth of the potential temperature $\theta = 2^{\circ}\text{C}$ isotherm, respectively. The 3500-m depth level, which is close to the boundary between NADW and AABW and which is also the approximate depth of current reversal at mooring VE, with a change in the direction of the mean flow from 151° at depth 2900 m to 332° at 3850 m , leads to a mean transport of $5.4 \pm 2.2 \text{ Sv}$. The more commonly used boundary at $\theta = 2^{\circ}\text{C}$ results in a somewhat larger mean value of $6.4 \pm 3.0 \text{ Sv}$. The mean value is influenced by some quite high daily values (see histogram in Fig. 5), the median value is therefore smaller. The given error bounds represent the standard deviations of the daily transports and therefore do not reflect possible errors due to the necessarily somewhat arbitrary choice of the cross-sectional areas. An error of 1 km in the width of each box is equivalent to 0.23 Sv or, assuming a 5% error in the areas, the

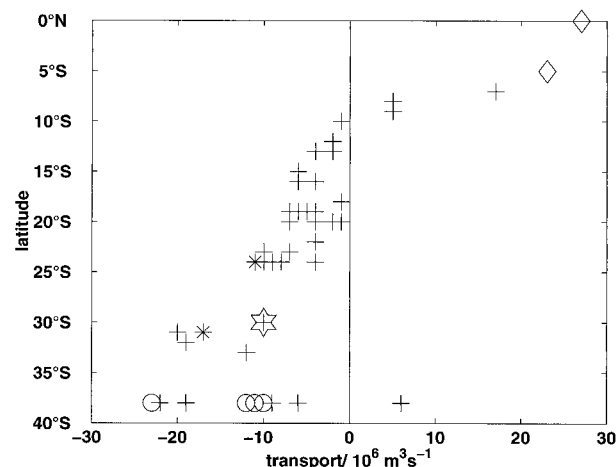


FIG. 4. Volume transport of the upper western boundary current in the South Atlantic. Crosses represent geostrophic calculations, stars are values inferred from current profilers, diamonds from direct current measurements, open circles from inverted echo sounders [from a compilation by Onken (1994)]. Our value is represented by a large open star.

TABLE 5. Minimum and maximum pressure observed by the upper instruments of the Vema channel moorings VW, VE, and DBK; mean speeds and directions; minimum and maximum temperatures; and the assumed cross-sectional width (see text).

Mooring name	Nominal depth (m)	Pressure		Mean speed cm s^{-1}	Mean direction (deg)	Temperature		Width (km)
		Minimum (dbar)	Maximum (dbar)			Minimum ($^{\circ}\text{C}$)	Maximum ($^{\circ}\text{C}$)	
VW	425	422	434	3.76	286	11.65	13.76	32.5
VW	840	836	846	1.60	258	4.51	5.98	32.5
VW	2970	—	—	0.67	36	2.67	2.82	32.5
VW	3590	—	—	3.55	338	0.83	1.88	32.5
VE	720	692	801	3.28	277	8.14	11.29	44
VE	1100	1065	1140	1.54	267	3.65	4.60	44
VE	2900	—	—	2.49	151	3.03	3.23	44
VE	3850	—	—	3.98	332	1.29	2.00	44
VE	4150	—	—	17.88	319	0.54	1.14	40
VE	4425	—	—	36.20	339	0.23	0.32	17
VE	4625	—	—	30.03	347	-0.19	-0.10	14
DBK	525	—	—	1.89	277	9.08	11.82	57
DBK	925	918	929	3.93	338	3.67	4.73	57
DBK	3025	—	—	1.44	243	2.63	2.89	57
DBK	3602	—	—	4.22	186	1.51	2.30	57

transport changes by 0.35 Sv. The AABW transports determined here are somewhat larger than the $4 \text{ Sv} \pm 1.2 \text{ Sv}$ obtained by Hogg et al. (1999) for the Vema Channel.

3. The method of flux determination

a. Individual sections

Property concentrations per mass (in g kg^{-1} $\mu\text{mol kg}^{-1}$, etc.) refer to a parameter P . The corresponding advective flux T_P through a cross-sectional area bounded by vertical boundaries z_1 and z_2 and horizontal boundaries x_1 and x_2 is then given by

$$T_P = \int_{z_1}^{z_2} \int_{x_1}^{x_2} \rho P v \, \delta z \, \delta x,$$

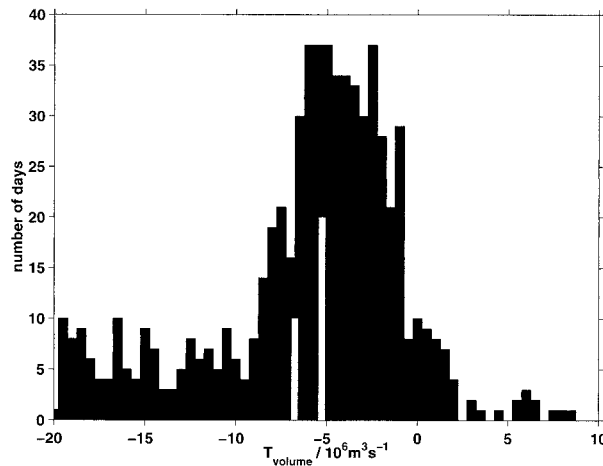


FIG. 5. Histogram of the daily volume transports of AABW through the Vema Channel with an upper boundary at $\theta = 2.0^{\circ}\text{C}$. The large white bar indicates the median, the smaller bar the mean value.

where ρ is density and v is the velocity normal to the cross section. We obtain the total meridional transport of P at a selected latitude in the South Atlantic if we integrate from surface ($z_1 = 0$) to bottom ($z_2 = H$) and from the continental margin of Africa in the east ($x_1 = x_e$) to the continental margin of South America in the west ($x_2 = x_w$). For the approximation of the integral by a sum of individual station pairs, a dense data coverage in the vertical and horizontal is required, as will be explained in section 4b.

We obtain the absolute heat transport T_{heat} with the parameter $P = \theta c_p$ (where c_p is the specific heat at constant pressure) with the condition that the total mass transport equals zero (Bryan 1962):

$$T_{\text{heat}} = \int_{\lambda_1}^{\lambda_2} \int_0^H \theta \rho c_p v \, \delta z \, \delta x.$$

We will use superscripts denoting a certain part of the flux (Ekman, baroclinic, etc.) and subscripts denoting the property advected.

The terms θ , ρ , and c_p can be calculated from CTD measurements, and other properties can also be determined from CTD measurements (salt, oxygen) or can be taken from bottle data and then be interpolated corresponding to CTD measurements (Holfort et al. 1998).

The ocean can be assumed to be close to geostrophic balance with the exception of the directly wind-induced currents in the Ekman layer of thickness H^{Ekman} . The velocity field can therefore be represented by a superposition of the Ekman velocity v^{Ekman} and the geostrophic velocity, which is decomposed into a depth-independent barotropic (\bar{v}) and a depth-dependent baroclinic (v') part. The heat transport is then given by

$$\begin{aligned}
T_{\text{heat}} = & \int_{\lambda_1}^{\lambda_2} \int_0^{H^{\text{Ekman}}} \theta \rho c_p v^{\text{Ekman}} \delta z \delta x \\
& + \int_{\lambda_1}^{\lambda_2} \int_0^H \theta \rho c_p \bar{v} \delta z \delta x \\
& + \int_{\lambda_1}^{\lambda_2} \int_0^H \theta \rho c_p v' \delta z \delta x.
\end{aligned}$$

This equation corresponds to the method used by Hall and Bryden (1982) in the North Atlantic for the region outside the western boundary current zone. In addition they considered the flux in the western boundary region of the Florida Current where a strong barotropic signal occurs over shallow topography and where $\int_0^H \theta \delta z$ will be significantly different from the section mean temperature. It is, however, well known that the Brazil Current transport in the subtropical South Atlantic is generally much weaker than that of the Florida Current and that it is predominantly baroclinic. We therefore assume the above equation to be valid for the whole cross section.

The barotropic velocity is separated into several components in order to facilitate the computation and the discussion of results. First a barotropic component \bar{v}^{LNM} is determined by specifying an initial level of no motion (LNM). The net mass transport across the section resulting from \bar{v}^{LNM} is compensated by a velocity component \bar{v}^{comp} , which is uniform over the whole section. This usually leads to motion at the initial LNM. Similarly we first determine the local Ekman velocity v^{Ekman} and compensate the resulting net mass flux by a horizontally uniform barotropic component \bar{v}^{Ekman} . The requirement of zero net mass transport through each zonal section is only a first approximation because of the neglect of the flow through Bering Strait and the mass flux due to runoff, precipitation, and evaporation ($RP - E$). A better constraint is therefore provided by setting the meridional salt flux through the Atlantic equal to the salt flux through Bering Strait because the freshwater fluxes $RP - E$ do not change the total amount of salt. We take account of this net mass transport by an additional uniform barotropic velocity \bar{v}^{salt} . The values of the heat transport, however, are always calculated without considering this component. It was shown by Warren (1999) that in this case the result is a good measure of the total energy transport in the ocean.

The velocity v^{Ekman} at each station pair is obtained from annual mean wind stress data by distributing the transport in the Ekman layer over the upper 50 m of the water column. We use data from two different climatologies: 1) Hellermann and Rosenstein (1983, hereafter HR) and 2) Southampton Oceanography Centre (SOC: Josey et al. 1996; see also <http://www.soc.soton.ac.uk/JRD/MET/fluxclimatology.html>). The Ekman transport T^{Ekman} results from v^{Ekman} and \bar{v}^{Ekman} . Results from an eddy-resolving Community

Modeling Experiment model (Böning 1992) showed that the effect of the annual cycle of the Ekman heat transport on the determination of the mean annual heat transport is small. This means, that the annual variations of $T_{\text{heat}}^{\text{Ekman}}$ (between -0.8 and 1.5 PW at 11°S) go into short-term storage, not affecting the annual mean transport. For a steady-state calculation as done here, it is therefore important to use the annual-mean wind stress and not the actually measured wind stress or the mean wind stress of the corresponding month.

Geostrophic shear calculations are only possible to the deepest common measurement depth at two stations. Below this depth we assume that the velocity decreases linearly, reaching zero at a preset distance (usually 1000 m) below the deepest common depth and then being constant. For other properties (e.g., temperature, silica) the shallower profile is extrapolated assuming that the difference in the property value between the two stations at the deepest common depth decrease linearly to zero with the same depth scale as the velocity (see Fig. 6). Between the deepest measurement and the bottom all values are assumed to be constant. A linear bottom profile is assumed between the two stations, thus forming the bottom triangle.

We want to demonstrate at one selected section (19°S) what order of magnitude of property transport can be expected for the different components. We assume the following: the meridional overturning rate is 15 Tg s^{-1} ; the barotropic part of \bar{v}^{LNM} and \bar{v}^{comp} corresponds to a horizontal transport of 45 Tg s^{-1} ; a measure of a typical property change in the vertical is the standard deviation of 100 dbar layer means and in the horizontal the standard deviation of the vertical mean; transports associated with the net mass transport across the section are given by the Bering Strait transport of 0.8 Tg s^{-1} (Coachman and Aagaard 1988) and the section mean concentration; the Ekman property transport is the mass transport in the Ekman layer times the concentration difference between Ekman layer and section mean.

Table 6 gives the corresponding parameter values and the relative importance of the four components as percentages of the transport magnitude. With the section-mean salt concentration being about 35 and the maximum difference of the vertically integrated salt concentration about 0.35 (a factor of 100 smaller) a barotropic eddy has to have at least a transport of 100 Tg s^{-1} to result in the same net salt transport as an overall net mass flux of 1 Tg s^{-1} .

Apart from salt and total carbon transports, which are given mainly by the section-mean mass transport, all property transports except for oxygen are dominated by the baroclinic and Ekman components. This results in a higher accuracy of transport estimates at sections with a low Ekman mass transport (i.e., 30°S as opposed to 11°S , see Table 10) because the baroclinic transport, determined from the density field, is better known than the barotropic transport.

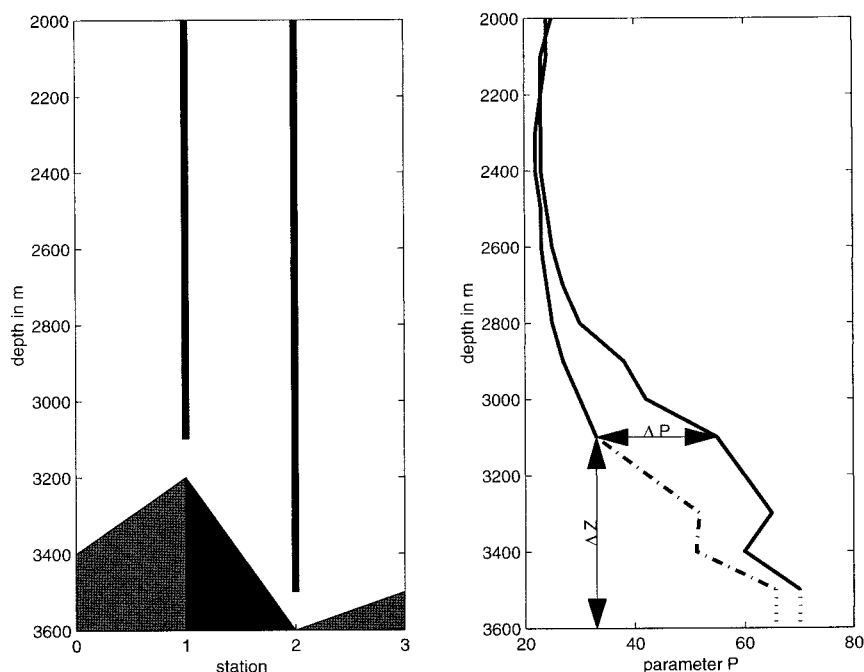


FIG. 6. Example of the bottom triangle and how the profiles were extrapolated to the bottom.

b. Inverse method using a set of sections

The inverse method as usually applied in oceanography (Wunsch 1978) assures that a chosen set of barotropic velocities satisfies certain linear constraints on the flow. These constraints are used to set up a system of linear equations for the unknown velocities \mathbf{v} :

$$A\mathbf{v} \sim \mathbf{b}.$$

With a sufficient number of well-behaving equations the system could be solved exactly. In reality, however, the linear constraints are only approximations with certain error margins. An exact solution, if found, is only exact in a mathematical sense but may give an unrealistic circulation due to the amplification of errors in measurements and assumptions. An exact solution is therefore not sought. Instead we search for a solution that minimizes the deviations from an initial state using

a singular value decomposition technique. The initial states are defined by the LNM assumptions with the known velocity parts \mathbf{v}' , $\mathbf{v}^{\text{Ekman}}$, and $\bar{\mathbf{v}}^{\text{LNM}}$. We search for the unknown barotropic velocity component $\bar{\mathbf{v}}^{\text{mod}} = \mathbf{v} - \mathbf{v}' - \mathbf{v}^{\text{Ekman}} - \bar{\mathbf{v}}^{\text{LNM}}$.

4. Constraints and error sources

a. Overview

In this section we present the constraints used in the inverse model and discuss some error sources. Errors due to measurement, spatial resolution, temporal variability, and differences in wind stress climatologies are discussed here mainly in the context of individual sections and not within the framework of the inverse model. Table 7 summarizes typical changes.

TABLE 6. The standard deviations δ of the vertical or horizontal variability, the section and Ekman layer mean values of different properties for WOCE section A9 (19°S, see text), and the percentage of the respective transports T relative to the total transport magnitude (C_{anthro} : anthropogenic carbon).

Property	Units	Baroclinic vertical δ	Percent of T	Horizontal δ	Percent of T	Barotropic section mean	Percent of T	Ekman mean	Percent of T
θ	°C	4.03	26	0.78	17	4.04	1	24.89	56
Salt		0.31	10	0.04	4	34.88	61	36.67	24
O ₂	$\mu\text{mol kg}^{-1}$	29.87	36	11.81	47	216.80	14	209.95	3
DIC	$\mu\text{mol kg}^{-1}$	29.71	12	12.76	18	2193.4	49	2069.8	21
NO ₃	$\mu\text{mol kg}^{-1}$	5.39	25	1.51	24	23.94	6	0.60	45
PO ₄	$\mu\text{mol kg}^{-1}$	0.34	27	0.08	21	1.61	7	0.21	46
SiO ₄	$\mu\text{mol kg}^{-1}$	22.55	36	6.32	34	39.74	3	0.66	26
C _{anthro}	$\mu\text{mol kg}^{-1}$	11.43	28	2.43	20	10.66	1	60.45	51

TABLE 7. Typical changes in meridional heat transports resulting from different assumptions and from changes in the constraints of the inverse system (see text). Total errors are calculated assuming the individual errors to be independent.

Error source	T_{heat} (PW) A8	T_{heat} (PW) A10
Errors outside inverse method		
Measurement error	<0.01	<0.01
Spatial resolution	<0.05	<0.05
Temporal variability	0.20	0.20
Wind stress	0.23	0.05
Total	0.31	0.21
Errors from inverse method		
Boundary current/shelf flow	0.08	0.09
AABW transport	0.03	0.03
PO4 transport	0.04	0.04
Velocity scaling	0.05	0.05
Equation weighting	0.03	0.03
Total	0.11	0.11
Overall total	0.33	0.24

b. Initial level of no motion

The selection of an initial LNM determines the barotropic velocity. Different LNMs were chosen, from levels based on water mass interfaces to a rather arbitrary set created by simply selecting constant pressure levels at every 400 dbar, and they gave a wide range of transport values. As will be expected, the majority of these LNMs result in mass or salt transports, which are incompatible with prior knowledge (e.g., that AABW is flowing northward). In order to further narrow down the choices, we can define an LNM to be *reasonable* if it meets certain criteria for the meridional overturning flow. We will not rationalize our criteria for *reasonable* circulations, the specifics for the criteria are also not that important. The effect is always to narrow down the solution range of the meridional transports. The criteria are

- the flow of Antarctic Bottom Water ($\sigma_4 > 45.92$) is northward;
- lower North Atlantic Deep Water ($\sigma_2 > 37.07$ and $\sigma_4 < 45.92$) flows southward;
- the flow of upper North Atlantic Deep Water ($\sigma_2 > 36.9$ and $\sigma_2 < 37.07$) is at least 5 Sv to the south;
- the total transport of North Atlantic Deep Water is less than 26 Sv; and

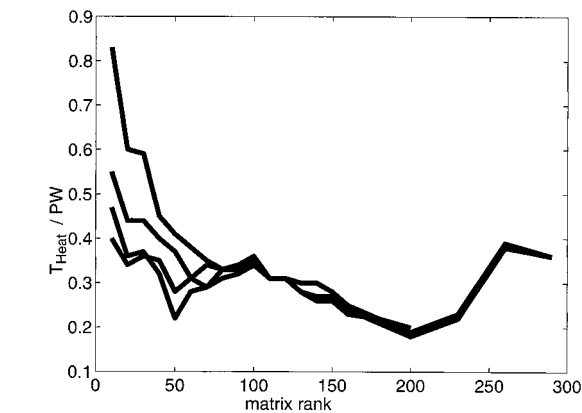


FIG. 7. Heat transport (T_{heat}) for the A10 section as a function of the matrix rank used in the inverse calculation. The different lines represent different initial LNMs in the same inverse model.

- the Antarctic Intermediate Water ($26.8 < \sigma_0 < 27.4$) flows northward.

Although this already reduces the range in the obtained transport numbers, the variability is still high (for T_{heat} about 0.2 PW). The inverse models change the velocities at these initial LNMs and with increasing rank the importance of the choice of the initial LNM is reduced. Figure 7 shows the heat transport as a function of matrix rank when using the same inverse model, but different a priori LNMs. Differences due to the initial state decrease with increasing matrix rank and are small for ranks above 80 to 100. It will be shown in section 5 that solutions at very low and high matrix ranks are not acceptable for different reasons. Therefore, the specifics of the LNM used are not very important for the meridional transport determination, and in the following we will present mostly results from a single LNM based on water mass characteristics. The choices of this LNM are given in Table 8. In the Angola Basin we take the same LNM as Warren and Speer (1991). In the other regions, the LNM usually lies either between AAIW and NADW or between NADW and AABW, with jumps occurring when changing from one of these interfaces to the other.

TABLE 8. Main LNMs used in the inverse analysis as a function of latitude (as given above) and longitude (P gives pressure in dbar).

8°–15°S	15°–21°S	21°–25°S	25°–50°S
10.2°–15.0°E $P = 4000$	17.0°W–20.0°E $\sigma_2 = 36.85$	5.0°W–20.0°E $\sigma_2 = 36.84$	14.0°W–20.0°E $\sigma_2 = 36.90$
16.2°W–10.2°E $P = 2400$	18.0°–17.0°W $\sigma_2 = 36.70$	16.0°–5.0°W $\sigma_2 = 36.86$	30.0°–14.0°W $\sigma_4 = 45.94$
35.2°–16.2°W $\sigma_0 = 27.881$	29.5°–18.0°W $P = 4450$	33.0°–16.0°W $P = 4300$	37.5°–30.0°W $\sigma_2 = 36.90$
40.0°–35.2°W bottom	32.0°–29.5°W $P = 4200$	34.0°–33.0°W $P = 4050$	43.5°–37.5°W $\sigma_4 = 45.94$
	60.0°–32.0°W $P = 4500$	35.0°–34.0°W $P = 3920$	60.0°–43.5°W $\sigma_2 = 36.90$
		36.0°–35.0°W $P = 3880$	
		37.0°–36.0°W $P = 3820$	
		40.0°–37.0°W $P = 3220$	
		60.0°–40.0°W $P = 1400$	

c. Measurements

Errors due to the uncertainty in pressure, temperature, and salinity measurements are negligible in this context. Differences in the heat transport due to an error of 0.002°C in temperature, 0.002 in salinity, and of 0.1% of the measured pressure are smaller than 0.005 PW, or only about 1% of the total heat transport.

Bottle data were interpolated onto the CTD data by using multiple linear regression. In this way we minimize errors in transport estimates due to insufficient spatial resolution, but we get an additional interpolation error. This error has the same order of magnitude as the measurement uncertainties (see Holfort et al. 1998) and is thus also small compared to other errors. When using nutrients as tracers, another type of uncertainty occurs. We discuss phosphate as an example. Although most of the phosphate occurs in dissolved inorganic form (DIP), some percentage also exists in dissolved organic form and/or as particulate material, and the different forms are related through the biological cycles. Apart from the euphotic layer, however, where the concentration of DIP is generally small and dissolved organic phosphorus can become important, the total phosphorus mostly occurs in the form of DIP, and the concentrations of the two other forms are very low and comparable to the uncertainty in DIP. We will include an estimate of the transport due to dissolved organic phosphorus in our phosphate constraint (see Holfort et al. 1998) but will otherwise neglect these contributions to the nutrient transport.

d. Spatial resolution

The integrations for determining transports have to be replaced by sums when considering station distances. An average number of about 100 stations per zonal section provides a typical station distance between 30 and 80 km, with most pairs sufficiently close to resolve the principal eddy scales [the first internal Rossby radius of deformation is in the range 30 km (30°S) to 80 km (10°S), Houry et al. (1987)]. In order to assess the effect of decreasing spatial resolution, we use various subsets of the stations (Table 9). When using only every other station, for example, the heat transport differences to the full-resolution set range from -0.07 to $+0.14$ PW. We can expect that deviations will be much smaller once we reach the eddy resolution. We therefore assume an error due to station resolution of <0.05 PW. The IGY data have about half the horizontal resolution of the WOCE data and are expected to have about twice this error. An additional error will occur with bottle data due to the much lower vertical resolution compared to the CTD data. The heat transport values obtained using only bottle data (using every station and up to 36 bottles per station) differ from the CTD data results by up to 0.1 PW. No systematic trend to lower or higher transport values for lower resolution data was found.

TABLE 9. Meridional heat transport calculated with full horizontal resolution and with subsampling. For example, a horizontal resolution of 1/3 means that only every third station was used. Vertical subsampling was done by interpolating the CTD data onto the standard depths of the NODC or the standard depths of the *METEOR* 1925/27 dataset (Wüst 1932).

Hori- zonal resolu- tion	Vertical resolution	T_{heat} (PW) A8 (11°S)	T_{heat} (PW) A9 (19°S)	T_{heat} (PW) A10 (30°S)
1/1	2 dbar	-0.458	-0.743	-0.462
1/2	2 dbar	-0.412	-0.794	-0.618
1/1	NODC	-0.435	-0.867	-0.487
1/2	NODC	-0.332	-0.862	-0.734
1/1	<i>Meteor</i>	-0.491	-0.843	-0.485
1/2	<i>Meteor</i>	-0.418	-0.908	-0.645
1/3	<i>Meteor</i>	-0.626	-0.847	-0.732

The influence of the bottom triangle is also related to the spatial resolution. The properties of the flow pattern below the deepest common depth have to be guessed. The two extreme cases of the scale of velocity decrease are no flow (0 m) or constant flow (10 000 m). These extremes lead to a difference of about 0.03 PW in the heat transport and 0.01 Tg s^{-1} in the mass transport of individual sections.

e. Temporal variability

There are no long-term time series to assess the temporal variability of the geostrophic transport, but some information on the temperature changes in time can be obtained through the comparison of sections taken at similar locations at different times. Comparing zonal sections with high quality data in the South Atlantic (*Meteor* 1925–27, IGY 1957–58, OCEANUS 1983, SAVE 1988–89, WOCE 1992–94), we find temperature differences on isobars of up to 0.5°C in the core of the NADW and up to 3°C in the surface layer. These changes are not necessarily long-term intrinsic temperature changes, Holfort et al. (2000) show for the 11°S sections that the changes in the deep ocean can be explained mostly by isopycnal up and down motion and lateral advection and mixing. Due to the high data quality, especially for the newer sections, measurement uncertainty is negligible (smaller than 0.01°C). Here we want to use this information for a rough estimate of temporal changes in the heat transport.

Assuming a southward NADW flow of 15 Tg s^{-1} compensated by a northward flow of 15 Tg s^{-1} in the surface waters, the heat transport changes are approximately 0.02 PW due to the temperature variability in the NADW and 0.18 PW due to the temperature variability of the surface waters.

The effects of the temporal variability of other parameters are more difficult to assess. The above temperature change will also affect the concentration of oxygen or CO_2 because of the temperature dependence of the solubility of gases. Also the effect of biological

TABLE 10. Mass transport in the Ekman layer ($T_{\text{mass}}^{\text{EKMAN}}$ in Tg s^{-1}) and the associated, mass compensated heat transport ($T_{\text{heat}}^{\text{EKMAN}}$ in PW) for the zonal sections using HR, respectively the SOC climatology.

Section	Latitude	HR		SOC	
		$T_{\text{mass}}^{\text{EKMAN}}$	$T_{\text{heat}}^{\text{EKMAN}}$	$T_{\text{mass}}^{\text{EKMAN}}$	$T_{\text{heat}}^{\text{EKMAN}}$
Oceanus	11°S	-11.72	-1.10	-9.23	-0.86
A8	11°S	-11.54	-1.10	-9.05	-0.86
A9	19°S	-6.19	-0.54	-5.08	-0.44
Oceanus	23°S	-3.69	-0.30	-3.06	-0.25
SAVE	25°S	-1.42	-0.12	-0.86	-0.07
A10	30°S	-0.35	-0.02	-0.20	-0.01
A11	40°S	+5.50	+0.23	+4.51	+0.19

activity can be relevant in the surface layer. Biological variability often has an annual cycle and will usually be high during plankton blooms. Datasets are not sufficiently detailed to assess these effects. However, we can hope for the overall effects to be small because the open South Atlantic is mostly oligotrophic. In the region of coastal upwelling near Africa the effect can be larger, but the area affected is relatively small, rendering the net effect also small. We would probably also find a larger effect in the region south of 30°S in the additional calculation done with the WOCE A11 section.

f. Wind stress

Errors due to Ekman transport uncertainties can arise from the temporal variability in the wind stress, from uncertainties in wind stress observations, and from the choice of the Ekman layer depth. To assess the effect of Ekman layer thickness on heat transport calculations, we vary the layer depth, normally chosen to be 50 m, between 20 and 100 m. Because of the larger absolute value of the Ekman transport at 11°S than at 30°S, the heat transport differences resulting from the different Ekman layer thicknesses are larger at 11°S (0.10 PW) than at 30°S (0.01 PW).

As discussed earlier we assume that the intraannual variations do not have a strong effect on the mean heat transport. If there should be such an effect, it will most probably have a greater influence at 11°S than at 30°S due to the larger wind stress variations at lower latitudes. If we assume that the intraannual variability causes a 10% change in the mean heat transport, we obtain differences of 0.02–0.04 PW.

Differences between the two wind stress climatologies (HR, SOC; see Table 10) are small at 30°S and, together with the smaller value of $1/f$ at this latitude, have only a minor influence (0.01 PW) on the 30°S estimates. At 11°S the SOC climatology has much lower wind stress than HR, and in combination with the larger value of $1/f$ a smaller southward Ekman mass transport results. Because the Ekman transport carries warm water southward, the decrease in the Ekman mass transport also implies a higher (+0.2 PW) northward heat transport. The changes at 19°S (+0.1 PW), 23°S (+0.05

PW), and 25°S (+0.03 PW) lie between the above extremes.

g. Net meridional salt flux

Given the volume transport of 0.8 Sv (Coachman and Aagaard 1988) and a mean salinity of 32.5 psu, the salt transport through Bering Strait provides approximately 26.7 Gg s^{-1} to the Atlantic. This must be balanced by a southward meridional salt transport across the zonal South Atlantic sections because salt is conserved. Here it is important to differentiate between salt and salinity. Salt has no sources and sinks and therefore is conservative. While conserving salt, it is possible to change the salinity by adding or removing freshwater: i.e., at Gibraltar the water flowing into the Mediterranean has a lower salinity than water leaving the Mediterranean at Gibraltar, but the same amount of salt that enters also exits the Mediterranean because more low salinity water flows into the Mediterranean than high salinity water flows out. The difference in mass transport leaves the Mediterranean with a salinity of zero through the air–sea interface. The small error (0.2 Gg s^{-1}), and therefore large importance, given to these constraints (one for each zonal section) emphasizes the fact that the net meridional salt transport has to be the same for all sections and does not reflect so much the actual uncertainty in the value of 26.7 Gg s^{-1} . Seasonal changes are neglected, similar to those in the Ekman transport, for a quasi-steady state. Interannual changes in volume transport through Bering Strait ($\pm 0.2 \text{ Sv}$; Coachman and Aagaard 1988; Roach et al. 1995), with a change of 0.1 Sv corresponding to a salt transport change of $\pm 3.2 \text{ Gg s}^{-1}$ have only minor effects on the meridional transports of all parameters except for mass and DIC (see also Table 6). The transports at all sections are influenced in a similar way, so these property transport changes just represent more or less water circulating in a closed loop around the American continent and therefore do not significantly influence transport divergences, which are important for the calculation of the air–sea fluxes. Differences in the net mass transport resulting from freshwater fluxes (evaporation, precipitation, and river runoff), however, can be relevant, for example, in the case of total carbon (Holfort et al. 1998).

h. Property conservation in layers

The main assumptions are that the flow occurs in layers between isopycnal surfaces, that the ocean is in steady state, and that salt is conserved in the layers. From these assumptions, the net salt flux into a closed box bounded vertically by two density surfaces and horizontally by hydrographic sections and/or by land must be zero. This holds for every pair of density surfaces resulting in one equation per layer in each box. The individual coefficients of the matrix (**A**) then correspond to the area integral of the density times salinity between

the respective isopycnic surfaces for the respective stations.

In contrast to previous workers (Fu 1981; Roemmich 1983), we use constraints for salt preservation instead of mass preservation. This is of advantage, as explained earlier, in the case of the total meridional transport. When considering isopycnal layers in restricted boxes, the isopycnal salinity changes will be sufficiently small to render a salt or mass preservation constraint equivalent. For simplicity, we use the salt preservation throughout the analysis.

In the horizontal, the boxes are bounded by hydrographic sections. The boxes used can be seen in Fig. 1. Six main boxes are defined by the seven zonal sections, and these main boxes are divided by the meridional sections into secondary boxes. Some of these secondary boxes do not provide additional information because the corresponding equations are linearly dependent (e.g., if we demand salt balance in the main box 25°–30°S and in the two secondary boxes in the west and in the east within this main box, it follows that the secondary box in the middle must also be in salt balance). We therefore excluded one of the secondary boxes of each main box. Because we then cannot specify the errors associated with this box, the implied error is a combination of the errors of the linearly dependent main and secondary boxes. This implied error is generally higher than the errors specified for the secondary boxes that were included in the calculation. Therefore the secondary box that was left out was, where possible, a box away from the boundaries formed by four sections. The error of such a box can be expected to be larger than a box including a solid boundary where the flow is known to be zero.

In the vertical, the boundaries are defined by density surfaces through which no exchange is allowed. It is emphasized that, because of the minimization method, the solutions of the linear system are not exact and therefore some diapycnal transports will exist in the solutions. The number of density layers has to be chosen as to be large enough for minimizing loss of information, and sufficiently small to prevent the amplification of uncertainties. The main calculations were performed using the density layers given in Table 2, but other calculations were also performed using the 18 layers defined by Macdonald (1993). These calculations gave similar results. Some preliminary calculations were also performed using other layer definitions, namely the eight layers defined by Roemmich (1983) or other layers of our own choice. Also, excluding one meridional section did not change the meridional transports considerably.

All these calculations indicated that details of layer definitions, considering the described constraints and the effect of matrix rank variations to be discussed later, are not crucial. We will therefore restrict the following presentation to the results from the main calculations.

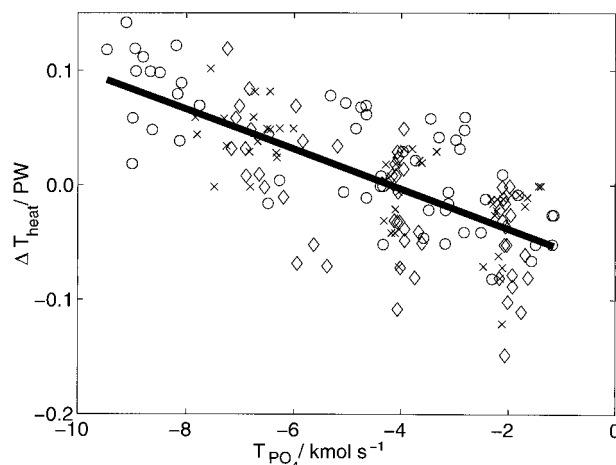


FIG. 8. Northward ΔT_{heat} as a function of northward T_{PO_4} at all six sections at ranks from 70 to 180 for models with different constraints on T_{PO_4} . Here ΔT_{heat} is the deviation in T_{heat} from the mean value of the respective section. The fitted line has a slope of $-0.02 \text{ PW kmol}^{-1} \text{ s}$. The different markers show the matrix ranks of the solution. Circle: $70 < \text{rank} < 105$; cross: $105 < \text{rank} < 135$; diamond: $135 < \text{rank} < 180$.

i. Net meridional phosphate flux

Keeling and Peng (1995) applied the constraint that the net meridional transport of phosphate across the equator should be equal to the phosphate transport through Bering Strait (about 1.7 kmol s^{-1}). We use the following alternatives:

- no constraint on the phosphate transport
- 2 kmol s^{-1} southward phosphate transport at all zonal sections [similar to Keeling and Peng (1995)]
- 4 kmol s^{-1} southward phosphate transport at all zonal sections, roughly accounting for total phosphate transport due to organic phosphorus (Holfort et al. 1998)
- zero phosphate divergence between zonal sections, thus determining the net phosphate transport across the zonal sections.

Using *reasonable* LNMs for individual zonal sections we find that the total southward phosphate transport across the sections is close to $2\text{--}4 \text{ kmol s}^{-1}$ and does not vary much from one section to the next at low latitudes. The southward transport is higher at 30°S . We will therefore expect significant changes in transport of other properties using the phosphate constraint in the inverse model at that latitude.

Figure 8 shows the relation between T_{PO_4} from the inverse model and the corresponding heat transport at 30°S for three model realizations with differing T_{PO_4} constraints and for a wide range of matrix ranks. Table 11 gives correlation coefficients and slopes of a linear regression between all the different transports from these model realizations. In general, property transports are well correlated if the parameter concentrations are well correlated, as is the case for phosphate and nitrate where the correlation coefficient for all six sections lies

TABLE 11. Correlation matrix for WOCE section A10 at 30°S of property transports over a wide range of matrix ranks for three inverse models with different T_{PO_4} constraints (upper matrix) and the respective slopes of a linear regression between transports (lower matrix). The upper-right corner of the slope matrix gives the slopes for the column parameters against the row parameters (i.e., $T_{\text{NO}_3} = \alpha + 14.32 \times T_{\text{PO}_4}$) and the lower-left corner the slopes for the regression of row against column parameter.

Parameter	Mass	Heat	Salt	O ₂	DIC	NO ₃	PO ₄	SiO ₄	C _{anthro}
Upper matrix									
Mass	1.00	-0.95	0.50	-0.62	0.93	0.97	0.89	0.85	-0.83
Heat	-0.95	1.00	-0.44	0.49	-0.91	-0.94	-0.86	-0.82	0.88
Salt	0.50	-0.44	1.00	-0.20	0.35	0.50	0.34	0.31	-0.59
O ₂	-0.62	0.49	-0.20	1.00	-0.80	-0.60	-0.83	-0.88	0.26
DIC	0.93	-0.91	0.35	-0.80	1.00	0.90	0.99	0.97	-0.69
NO ₃	0.97	-0.94	0.50	-0.60	0.90	1.00	0.85	0.81	-0.87
PO ₄	0.89	-0.86	0.34	-0.83	0.99	0.85	1.00	0.98	-0.61
SiO ₄	0.85	-0.82	0.31	-0.88	0.97	0.81	0.98	1.00	-0.59
C _{anthro}	-0.83	0.88	-0.59	0.26	-0.69	-0.87	-0.61	-0.59	1.00
Lower matrix									
Mass	1.00	-0.64	0.26	-0.00	0.00	0.00	0.02	0.00	-0.00
Heat	-1.40	1.00	-0.33	0.00	-0.00	-0.00	-0.03	-0.00	0.00
Salt	0.96	-0.57	1.00	-0.00	0.00	0.00	0.01	0.00	-0.00
O ₂	-1904.46	1023.37	-321.38	1.00	-0.31	-2.14	-50.43	-0.82	0.72
DIC	7333.98	-4841.71	1439.32	-2.05	1.00	8.24	152.67	2.31	-4.89
NO ₃	837.65	-545.83	221.00	-0.17	0.10	1.00	14.32	0.21	-0.68
PO ₄	45.02	-29.70	9.02	-0.01	0.01	0.05	1.00	0.02	-0.03
SiO ₄	2800.02	-1827.51	528.03	-0.95	0.41	3.12	63.87	1.00	-1.76
C _{anthro}	-926.71	664.93	-339.78	0.09	-0.10	-1.13	-13.38	-0.20	1.00

between 0.85 and 1.00, with a slope ($T_{\text{NO}_3}/T_{\text{PO}_4}$) between 13.1 and 17.5, which is close to the Redfield ratio for these concentrations. The slope of $T_{\text{DIC}}/T_{\text{PO}_4}$ is higher than the Redfield ratio (110 to 153 vs 106), with the difference most probably being due to the solubility pump in the T_{DIC} . For most sections the correlation between T_{PO_4} and T_{heat} is similar to the value found at 30°S, with a slope of about $-0.02 \text{ PW/kmol s}^{-1}$. The heat transport estimate at 30°S from our standard inverse calculation, using a constraint $T_{\text{PO}_4} = -4 \text{ kmol s}^{-1}$, is smaller than the one obtained from the LNM approach, and also smaller than in the previous calculations by Holfort (1994), which did not constrain the T_{PO_4} . These solutions without this constraint had a T_{PO_4} of about -12 kmol s^{-1} , which is considered less realistic than a magnitude of $2\text{--}4 \text{ kmol s}^{-1}$ as discussed earlier. Using the above slope the difference in the T_{PO_4} represents a difference in the T_{heat} of $+0.16 \text{ PW}$ ($-8 \text{ kmol s}^{-1} \cdot -0.02 \text{ PW/kmol s}^{-1}$). This is significant in view of the inverse model error of about 0.1 PW given in Table 7. For the same reason we also find a lower T_{heat} here for WOCE section A11 at nominally 40°S than Saunders and King (1995).

j. Silica conservation

Silica can be expected to be a conservative property, like salt, to a good approximation. Although some silica recycling takes place in the ocean, the process of dissolution of opaline material is a slow process that occurs primarily in bottom sediments. In almost stagnant waters near the bottom sources and sinks can be more easily detected because they lead to concentration gradients in

the water column. But despite the poor ventilation of the eastern basin, we usually do not see an increase of silica content toward the bottom. The only exception is a narrow zone of high silica, high nutrient, and low oxygen concentration along the eastern continental slope at about 4000 m north of about 20°S. This was related to the dissolution of organic material from the Congo River plume by van Bennekom and Berger (1984). According to van Bennekom (1996), the flux in the Congo fan proper is about $20\text{--}50 \mu\text{mol cm}^{-2} \text{ yr}^{-1}$, but only $0.1\text{--}0.5 \mu\text{mol cm}^{-2} \text{ yr}^{-1}$ in the southern and western Angola Basin. An error of 5 kmol s^{-1} in the silica conservation, taken over an area of 1000 km by 1000 km is equivalent to $15.5 \mu\text{mol cm}^{-2} \text{ yr}^{-1}$. Although the flux per area is larger in the Congo Fan than this error, the dimension of the plume is sufficiently small compared to the above area. Apart from the Congo Fan, there are no known essential silica sources in the deep layers of the South Atlantic between 11° and 30°S, and we therefore have good reasons to impose silica conservation in the deeper layers.

The euphotic zone can act as a silica sink due to the formation of opaline material but, because surface concentrations of silica are low throughout the subtropical South Atlantic and silica bounding organisms are few, we also impose silica conservation in the upper layers, although not directly in the uppermost layer ($\sigma_0 < 26.6$). Such a constraint was also used by Macdonald (1993). The changes induced by the inclusion of the silica constraint are small (less than 0.05 PW in the heat transport) and are not distinguishable from related changes due to matrix rank. This can be explained by the linear correlation between salt and silica in the deep layers where

silica is high, which renders the equations for salt and silica linearly dependent.

k. Bottom water transport

Fluxes in the deep layers of the eastern South Atlantic are inhibited by the Walvis Ridge. The mass flux through the zonal sections east of the Mid-Atlantic Ridge in layers deeper than 3000–3500 m is therefore set to zero. Depending on the chosen model and the matrix rank the residuals for this constraint are usually smaller than 1 Tg s^{-1} , and no special error analysis was performed for this constraint.

l. Brazil Current transport

The constraint we chose on the basis of the direct transport estimates demands a southward Brazil Current mass transport of 10 Tg s^{-1} in the upper 600 m in the area of the 15 westernmost stations of section A10. In order to estimate uncertainties, we also made calculations prescribing a doubling of the transport or by reducing the effective cross section by one-half. This results in a heat transport change by not more than 0.03 PW at 30°S for matrix ranks from 120 to 200 (Fig. 10) and smaller deviations at lower latitudes. Brazil Current transport changes seem to be compensated by a rather local recirculation, to a large extent the changing Brazil Current mass transport is compensated by an opposite mass transport across the 30°S section just east of the Brazil Current. This compensating flow has temperature, salt, silica, etc., values comparable to the values in the Brazil Current. The combined transport of the Brazil Current and the recirculation across 30°S does not change considerably and therefore a change in the Brazil Current mass transport has a negligible effect on the transports across the other sections.

Another aspect is the possibility of unresolved flow over the shelf. In general the zonal sections start and end at the shelf edge near depths of about 100–200 m. Although the cross-sectional areas between the outer stations and the coast are small and therefore mass transport is also small even with high velocities, the associated heat transport can be substantial due to the high temperatures on the shelf. At 11°S Speer et al. (1996) concluded that the error in the heat transport due to the unresolved flow on the shelf is 0.08 PW per 1 Tg s^{-1} of shelf flow. This was based on a difference of 20°C between the mean temperature on the shelf and the section-mean temperature. We assume this value to be representative for the flow on the western shelf between 11° and 30°S . The error is somewhat lower at the eastern boundary (about 0.06 PW Tg^{-1}) due to the lower temperatures there. A larger error can be expected at 19°S because of a wider shelf with possibly larger mass transports.

m. AABW transport

The AABW flows from the Argentine to the Brazil Basin through Vema Channel (Hogg et al. 1982) and also through Hunter Channel (Speer et al. 1992; Speer and Zenk 1993; Hogg et al. 1999). We earlier described our method of calculating the AABW Vema Channel transports from the WOCE mooring data and will use a mass transport of 5 Tg s^{-1} here. Results on the Hunter Channel volume transport vary from 0.7 to 2.9 Sv . The recent results from moored current meters and hydrography (Hogg et al. 1999) give a total AABW volume transport of about 7 Sv . We therefore use 2 Tg s^{-1} for the Hunter Channel mass transport.

We consider negligible any transport changes due to the 1° of latitude separation of the line of moorings used for the above transport calculations in Vema Channel and the zonal 30°S section.

The mass transport in Vema Channel and the total transport were allowed to vary in the range 4–6 or 4–8 Tg s^{-1} , respectively. The typical deviation from the heat flux obtained with 5 and 7 Tg s^{-1} , respectively, is $\pm 0.04 \text{ PW}$. The variations of mass transports similarly affect the heat flux at all other sections. Although the mass transport is only constrained directly in certain layers at 30°S , the mass transports in these layers will also change in other sections due to the salt preservation (within some error) in layers because of the nearly linear relationship of salt and mass transport.

n. Addition of the A11 section

In additional inverse calculations we also included WOCE section A11, at nominally 40°S , with the constraints taken from Saunders and King (1995). There arise, however, difficulties when incorporating the A11 section in the inverse system as we use it. The region between A10 and A11 is a region of intense mixing (Brazil–Malvinas Confluence) and of water mass formation at the subtropical and polar fronts. It is not clear whether one may assume mass or salt preservation in isopycnal layers or whether cross-isopycnal velocities have to be considered explicitly. Similar difficulties can be expected when including WOCE section A6 (not done here) because of equatorial processes.

5. Inverse model

The constraints determine the set of linear equations that have to be solved. The system is underdetermined. The relative importance of equations is expressed by the weighting, and the scaling gives the relative importance of unknowns. The matrix rank determines the importance of the inverse system compared to the initial conditions as described below. The choice from the many possible solutions depends on the weighting and scaling of equations and the matrix rank used. Weights, scales, and matrix ranks are not independent of each

other. We give a simple explanation of the physical meaning in the following and then look into the details of one specific solution.

a. Weighting of equations

As mentioned before, the equations describe the physical constraints. They are not solved exactly, but only within a given uncertainty, and the solution minimizes the sum of the squares of numerical values of these uncertainties. We emphasize the numerical values here because the physical constraint does not change if mass conservation is expressed in kilograms per second or grams per day, but the numerical values do. The weighting is just a factor for each equation, and we use it to decide which numerical values of the uncertainties of different equations are regarded as “equal.” For example, an error of 1 (dimensionless) in the weighted equations may correspond to 3.5 Gg s^{-1} salt divergence in one equation, to 6 kmol s^{-1} of silica divergence in another, to 20 Tg s^{-1} of mass transport in a third equation, etc.. The equations were weighted first based on the magnitude of their coefficients (i.e., maximum absolute value or mean absolute value) and then weighted according to an a priori estimate of the uncertainty in the constraints (for the specific section 5d see Table 13).

In general we assume a smaller error for the conservation equations in the main boxes than for the conservation in the secondary boxes. This lower importance of the secondary boxes is assumed because of the problem that exists in exactly matching the meridional and zonal sections. For example, in nonsynoptic sections an eddy can cause major deviations by occurring at the crossing point in one section and not the other.

The individual weights are checked against the residuals in the solution and, if the error in one equation is too high or low compared to the assumptions, the computation is repeated using a higher or lower weight for this equation. For a first set of inverse models this was done manually; later the final weights were obtained by an iterative process. The relative residuals (relative to the assumed error, i.e., residual/assumed error) for a solution of rank 120 were calculated. Equations with a residual smaller than 25% of the assumed error were given a lower weight; equations with a relative residual of more than twice the mean relative residual were given a higher weight. Using the new weights this step was iterated usually three times, but sometimes also up to ten times.

At low matrix ranks individual equations contribute more to the solution than at higher ranks and therefore the weights have more influence. But at ranks of about 150, different initial weights of the equations, within reasonable limits, have only a minor influence on the calculated heat ($\pm 0.05 \text{ PW}$) and mass ($\pm 0.02 \text{ Tg s}^{-1}$) transport.

TABLE 12. Hydrographic sections of the model used for the statistics of the inverse solution. Also given are the corresponding column numbers of the velocities in matrix A, the assumed errors, and the scaling.

Section	Position	Direction	Columns	Scaling
Oceanus	11°S	East–west	001–077	$\text{AR}^{0.5}$, 1.0
A9	19°S	West–east	078–168	$\text{AR}^{0.5}$, 1.0
Oceanus	23°S	East–west	169–253	$\text{AR}^{0.5}$, 1.0
A10	30°S	West–east	254–363	$\text{AR}^{0.5}$, 1.0
A8	11°S	West–east	364–472	$\text{AR}^{0.5}$, 1.0
SAVE	25°S	West–east	473–525	$\text{AR}^{0.5}$, 2.5
A11	40°S	West–east	526–615	$\text{AR}^{0.5}$, 2.0
SAVE-6	25°W	South–north	616–665	$\text{AR}^{0.5}$, 2.0
Oceanus	30°W	North–south	666–680	$\text{AR}^{0.5}$, 1.5
(A9)	15°W	North–south	681–686	$\text{AR}^{0.5}$, 1.2
SAVE-3	00°W	South–north	687–702	$\text{AR}^{0.5}$, 4.5

b. Scaling of velocities

Scaling corresponds to the relative importance of the unknowns with respect to each other. One form of scaling is the use of different parameters as unknowns. For example, instead of using the barotropic velocity as an unknown, the same physical system can be described by using the net barotropic transports between stations as the unknowns by scaling the velocities with the total area (AR) of the corresponding station pair. Because the inverse method minimizes the deviations of the unknowns from the initial state, the solutions of the two alternative systems, both representing the same physical constraints, will be different. Our standard calculation is made by scaling with the square root of the total area ($\text{AR}^{0.5}$), not with $\text{AR}^0 = 1$, which corresponds to minimizing the velocity deviations, and not with $\text{AR}^1 = \text{AR}$, which corresponds to minimizing the transport deviations. This corresponds to minimizing the dynamic height difference between stations in the case where water depth equals station distance. In general the meridional sections and also sections with larger station spacing are given less importance. Apart from the resulting slight differences in the scaling of individual sections, all velocities are scaled in the same manner (see Table 12).

At the same matrix rank, changes due to different scaling range from minor ($\pm 0.03 \text{ PW}$ at 30°S) to substantial ($\pm 0.15 \text{ PW}$ at 11°S). But due to the scaling the velocities are larger in the case of minimizing the transports (standard deviation s with rank 150, $s = 0.16 \text{ m s}^{-1}$) than in the standard case ($s = 0.07 \text{ m s}^{-1}$) or in the case of minimizing the velocities ($s = 0.03 \text{ m s}^{-1}$). When the heat transport is plotted as a function of s (Fig. 9), the solutions calculated by minimizing the velocities/transport are similar to the standard solution at a lower/higher matrix rank. Differences between different scaling at the same s (up to about $s = 0.08 \text{ m s}^{-1}$) are of order $\pm 0.05 \text{ PW}$.

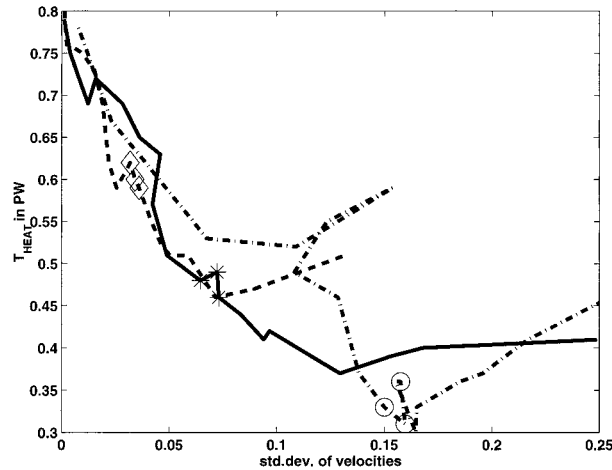


FIG. 9. Plot of T_{heat} at 11°S for different ranks with different scaling of the unknowns. The dashed line is the solution that minimizes the velocities (scaling with AR^0), the dash-dotted is with minimization of the transports (scaling with AR^1), and the solid line is with our standard scaling ($\text{AR}^{0.5}$). Markers show the solutions for ranks 140, 150, and 160 of the different scalings. The x axis is the standard deviation of the velocities of the solutions.

c. Matrix rank

The matrix rank expresses the relevance of the set of equations compared to the initial state. At a matrix rank of zero no equations are used for the solution, and we have the initial state. A higher rank gives a better agreement with the equations, but a greater deviation from the initial state. At much higher ranks the equations are solved rather precisely but, because the constraints are not an exact model of the real ocean and have uncertainties, as have our data, the errors are magnified and the solutions give unreasonably high barotropic velocities. The optimal rank, without losing too much information and still obtaining an acceptable noise level, cannot be determined objectively. For each inverse system we therefore calculated the solution for a wide range of ranks. In most cases a broad range of ranks could be found where several parameters of the solution (e.g., the heat and mass transport) showed only little variation.

The chosen matrix rank has a great influence on the calculated transports. Our typical inverse system has about 600 unknowns and 390 equations, and solutions were calculated for ranks up to 300. In general, residuals were high up to a rank of about 50. Differences due to the initial state, as seen in Fig. 7, which shows the heat transport as a function of matrix rank when using the same inverse system but different a priori LNMs, decreased as expected with increasing matrix rank and are small for ranks above 80–100. As discussed above, a higher rank increases the importance of equations compared to the initial state. If two models differ in the value of the imposed phosphate transport (e.g., 2 kmol s^{-1} and 4 kmol s^{-1}) both models will start (rank = 0) at the same phosphate transport given by the LNM calculation, but will end (full rank) at the respective phos-

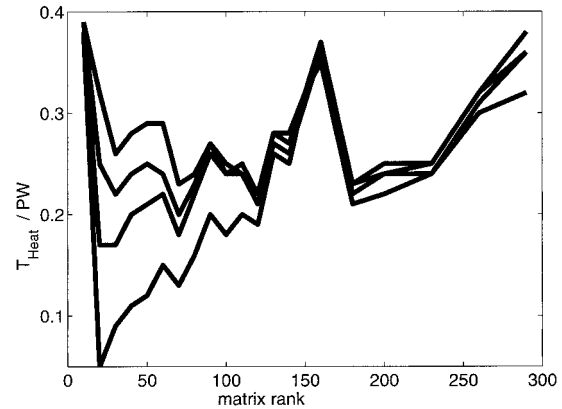


FIG. 10. Plot of T_{heat} at 30°S as a function of matrix rank for models with different constraints on the Brazil Current transport.

phate transport given by the constraint. As seen before, this also means different heat transports ($2 \times 0.02 \text{ PW kmol s}^{-1}$). If we change to constraints that do not correlate as well with the heat transport (e.g., the Brazil Current transport), the models generally show diverging net transports with increasing rank only up to a certain rank. Above, the change in constraints becomes less and less important and the net transports again converge as more constraints are incorporated in the solution (see Fig. 10).

We deduced our final solutions from the matrix rank in the case where differences due to initial state were small (rank > 80), where differences due to the inverse models used were small (rank < 200), and where transports were *stable* over a certain range of matrix ranks (see Fig. 11). No range can be found where all transports at all sections are *stable*, and as a compromise we took the mean value of the transports at ranks 140, 150, and 160.

Even with these rather high ranks the residuals are not all within the specified errors. Within the residuals we can find information about neglected terms, such as the exchange across isopycnals, in the constraints. It could be argued that with the assumed errors we are underestimating these diapycnal terms. These terms are not well known, but if we only consider the two sections near 11°S these terms can be neglected because the horizontal area between these two sections is very small. If one assumes that the solution at some rank gives the right velocity field at both sections, the differences in the calculated transports of individual layers and total heat transport ($T_{\text{heat}}^{\text{Oceanus}} = 0.79 \text{ PW}$, $T_{\text{heat}}^{\text{WOCEAS}} = 0.49 \text{ PW}$) are due to temporal variability. Assuming steady state, T_{heat} is constant and a very simple steady state inverse model is the overdetermined 2×1 system: $T_{\text{heat}} = 0.79 \text{ PW}$; $T_{\text{heat}} = 0.49 \text{ PW}$.

The solution of this inverse system (or a similar system with more sections) provides the mean of the individual T_{heat} values. We hope that also in a more complex inverse system, with both T_{heat} values at 11°S ap-

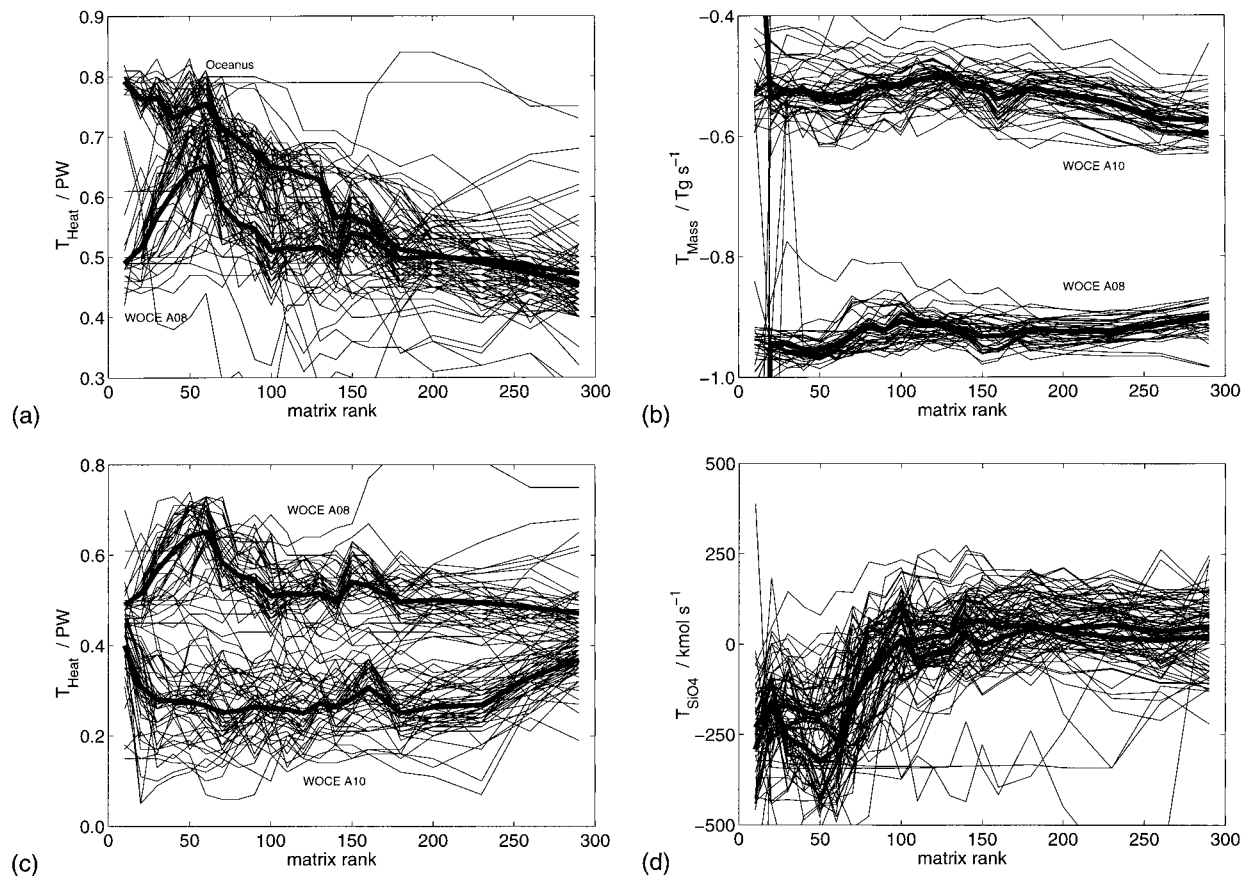


FIG. 11. Transports as a function of matrix rank for different models with the thick lines representing the mean value of all these models: (a) T_{heat} at the two 11°S sections (OCEANUS, A8), (b) T_{mass} at the sections at 11°S (A8) and 30°S (A10), (c) T_{heat} at the sections at 11°S (A8) and 30°S (A10), and (d) T_{SiO_4} at the sections at 11°S (A8) and 30°S (A10).

proaching the same value (see Fig. 11a) with increasing rank, this value will approach the true mean.

The standard deviation of the T_{heat} values of single inverse models at ranks 140 to 160 is about 0.03 PW, which we take as error due to matrix rank. Using a larger range of ranks (100–160) increases the standard deviation up to 0.1 PW.

d. A specific solution

From the numerous models used, we select one to present some characteristics of the inverse solution in more detail. The particular model chosen is one using all sections (including A11) and all constraints (including silica conservation in layers). The specific constraints are listed in Table 13. The given weights are the initial ones and the final weights were obtained by an iterative process. The mean relative residual for this specific model at rank 120 for the first iterative step was about 930%, whereas after 10 iterations the final mean relative error was 290%. Figure 12 compares the initial residual of the first iterative step with the final residuals at rank 120. As can be seen the initial residuals for some

equations were rather high, but the final residuals are smaller and had almost the same order of magnitude. Some of the very low final weights are due to linearly or almost linearly dependent equations. In such a case even with a weight equaling zero (meaning not using this equation at all) the solution is not affected. With increasing rank the residuals became smaller but the solution norm grows (Fig. 13, expressed as the standard deviation of the velocities). The expected error the velocity using the initial LNM is at most of the order of several centimeters per second, and ranks higher than 160 give unrealistically high velocities. The solution at rank 160 leads to a relative error of about 150%. We consider solutions with a rank between 120 and 160 as a good compromise between small residuals and small solution norm.

The individual velocities of the meridional sections are not well resolved (e.g., see row 673 of \mathbf{VV}^T in Fig. 14). Velocities from a meridional section providing a boundary of a secondary box are quite well correlated, and therefore only the mean gives useful information. This is most noticeable in the eastern basin. Due to the small spatial variability at depth, the coefficients of the

TABLE 13. Constraints of the model used for the statistics of the inverse solution. Also given are the corresponding row numbers of the equations in matrix A, the assumed errors, and the initial weighting of the equations.

Constraint	Error	Weight	Row
Salt conservation in six main boxes for 18 density layers ($\sigma_0 > 26.6$) and total transport	5.0 Gg s ⁻¹	Max	
Oceanus 11°S and WOCE A8		0.2	1–19
Oceanus 11°S and WOCE A9		0.25	20–38
WOCE A9 and Oceanus 23°S		0.25	39–57
Oceanus 23°S and SAVE 25°S		0.25	58–76
SAVE 25°S and WOCE A10		0.25	77–95
WOCE A10 and WOCE A11		0.35	96–114
Silica conservation in six main boxes for 18 density layers ($\sigma_0 > 26.6$) and total transport box scaling as in salt conservation	5.0 kmol s ⁻¹	Max	115–228
Salt conservation in 14 secondary boxes for 18 density layers ($\sigma_0 > 26.6$ and total transport)	6.0 Gg s ⁻¹	Max	229–459
7 Tg s ⁻¹ of AABW transport ($\sigma_4 > 45.93$) across 30°S	1.0 Tg s ⁻¹	Max	460
5 Tg s ⁻¹ of AABW transport ($\sigma_4 > 45.93$) between Brazil and the Rio Grande Rise at 30°S	1.0 Tg s ⁻¹	Max	461
10 Tg s ⁻¹ of Brazil current transport (depth 0–600 m) at 30°S	2.0 Tg s ⁻¹	Max	462
Zero net mass transport for layers $\sigma_3 > 41.5$ at zonal sections (11°–30°S) in the Angola Basin	0.8 Tg s ⁻¹	Max	463–479
Zero net mass transport for layers $\sigma_4 > 45.92$ at zonal sections (23°–40°S) in the Cape Basin	0.7 Tg s ⁻¹	Max	480–487
Net salt transport of –27.6 at all zonal sections	0.2 Gg s ⁻¹	Max, 0.01	488–494
Net phosphate transport of –4 kmol s ⁻¹ at all zonal sections	1.0 kmol s ⁻¹	Max	495–501
45 Tg s ⁻¹ western boundary current at WOCE A11	5.0 Tg s ⁻¹	Max	502
5 Tg s ⁻¹ eastern boundary current at WOCE A11	1.0 Tg s ⁻¹	Max	503
80 Tg s ⁻¹ Zapiola anticyclon at WOCE A11	20.0 Tg s ⁻¹	Max	504, 505

matrix are almost the same for different station pairs. In that case the solution with the minimum solution norm is a constant for all station pairs. The solutions of the zonal sections are generally better resolved (more pronounced peaks of \mathbf{UU}^T), more so in the western than in the eastern basin due to the low variability in the eastern basin.

The most notable correlations in the data resolution matrix (\mathbf{UU}^T , Fig. 15) are between the constraint of salt conservation in main boxes (Nos. 1–114 in Table 13) with the corresponding silica conservation (Nos. 115–228). This reflects the aforementioned good correlation between silica and salt. The fixed salt transport (Nos. 488–494) for all zonal sections implies total salt conservation. Therefore the equations constraining the total salt divergence in the main boxes (Nos. 19, 38, ...) are only linear combinations of the total salt transport equations and do not give additional information (diagonal elements of $\mathbf{UU}^T = 0$).

e. Diapycnal transports

One of the assumptions for the inverse model was that diapycnal transports are zero. It is known from earlier observations that diapycnal transports actually have to be expected. About 4 Sv of water with a temperature below 1°C enter the Brazil Basin from the south, but no water below 1°C leaves to the north (see Hogg et al. 1996). As a consequence all this water has to upwell through the 1°C isothermal surface (or through

an equivalent isopycnal surface). With an area of about 2500 km × 1500 km this results in a diapycnal velocity of about 1×10^{-4} cm s⁻¹. Diapycnal velocities of the same order of magnitude were also determined by MacDonald (1998). From the residuals in our solution we can calculate diapycnal transports. Mass transport convergence/divergence in the lowest layer between 11° and 30°S can only be compensated by an upward/downward transport between the two lowest layers. The net convergence/divergence of the two lowest layers has to be related to the transport into or out of the layer above. Continuing to the uppermost layer we obtain the transports across each layer boundary. The transport at the upper boundary is the total air–sea flux. The mean diapycnal velocities are small and of the expected order of magnitude, for example, a vertical mass transport of 1 Tg s⁻¹ or about 1 Sv of volume transport across an area of about 1000 km × 1000 km results in velocities of about 1×10^{-4} cm s⁻¹.

The mean diapycnal transports (Fig. 16) between 11° and 30°S are upward, increasing almost steadily toward the surface layer. The upward mass transports then decrease in the uppermost layer and arrive at a sea-to-air flux of about 0.4 Tg s⁻¹. The large mass divergence in the uppermost layer is due to the fact that the salt conservation in this layer is done only implicitly in the normal calculation. Imposing salt conservation in all layers below the uppermost layer and in the total transport renders the salt conservation equation in the up-

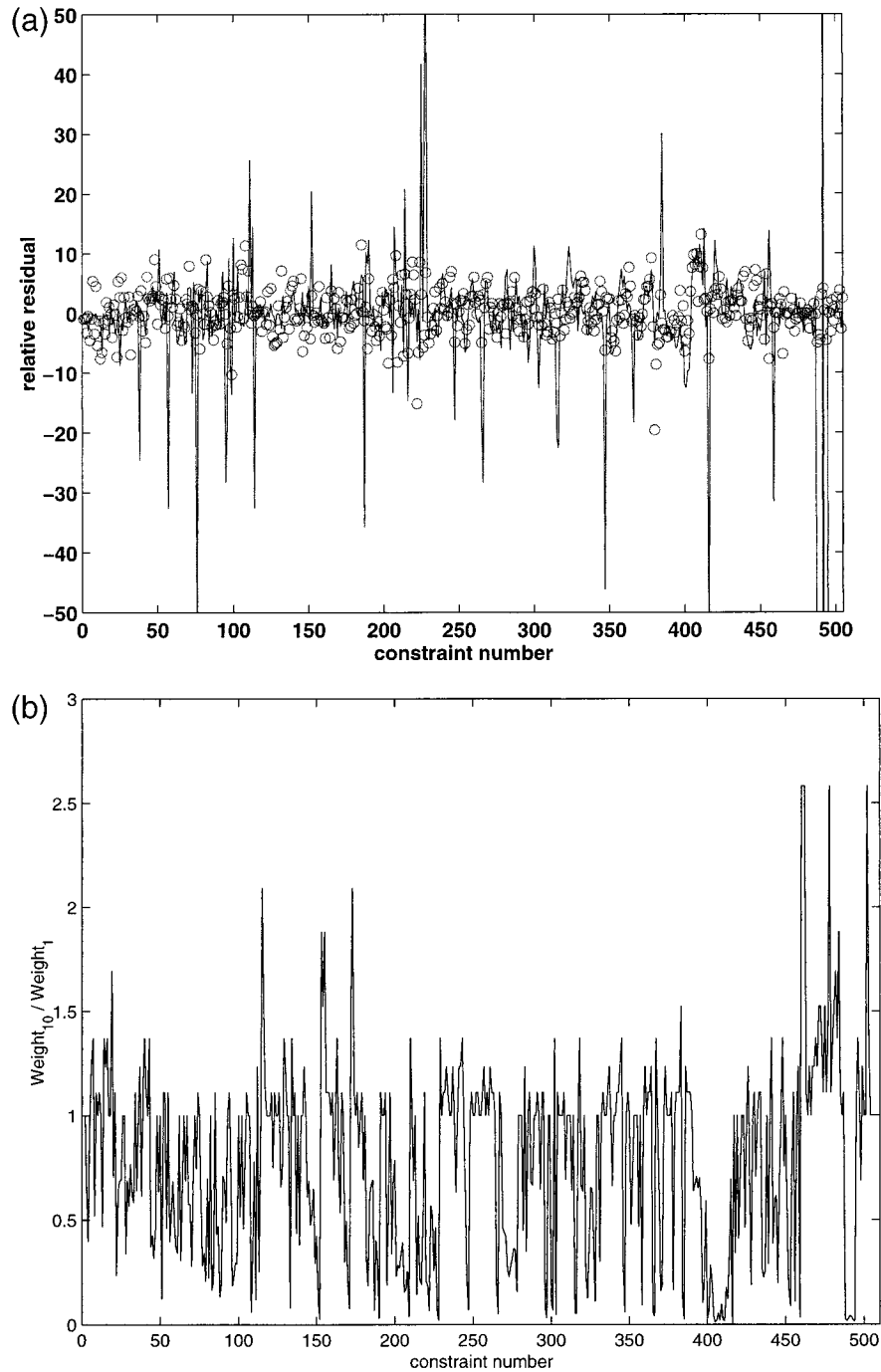


FIG. 12. (a) The relative residuals (residual divided by assumed error) of the constraints. The line gives the relative residuals at rank 120 of the initial weighting and the points shows the residuals after 10 iterations. (b) The ratio of the final weights after 10 iterations and the initial weights. Ratios below 1 mean lower final weights.

permost layer linearly dependent. If we do not use the salt conservation equation of the uppermost layer explicitly, we also cannot impose an error estimate for this equation, and the implicit error is approximately the sum of the errors in the other layers. If we use the uppermost layer salt conservation explicitly and assume the same

error in the upper layer as in the deeper layers, the diapycnal transports are quite different and the total heat transport is generally higher (about 0.1 PW, see Fig. 17) than in the normal calculation. With an error five times or more the error in the deeper layer we obtain almost the same result as in the normal calculation.

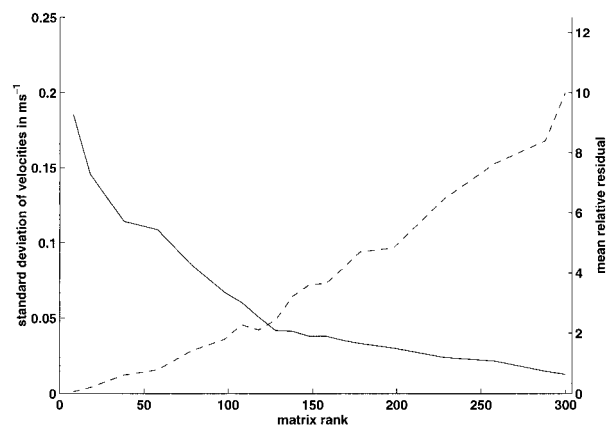


FIG. 13. The mean relative residual (solid line) and the standard deviation of the velocities (dashed line) as a function of matrix rank.

6. The meridional fluxes

The estimates of meridional fluxes between 11°S and nominally 40°S from our standard inverse calculation are given in Table 14 for the calculations using the Hellermann and Rosenstein (1983) wind stress data and also the SOC wind stress climatology. The values represent the mean of more than 100 different inverse model formulations at ranks 140, 150, and 160. The transport values with the SOC climatology and for the A11 section are based on a subset of inverse calculations. The standard deviation of the transport values of different inverse calculations can be seen as an error estimate. For T_{heat} the error increases from 0.05 PW at 30°S to 0.09 PW at 11°S, somewhat smaller errors than in the calculation of Table 7. To this error of the inverse model, we still have to add the error estimates associated with uncertainties in the wind stress and with temporal variability, both of them being considerably larger.

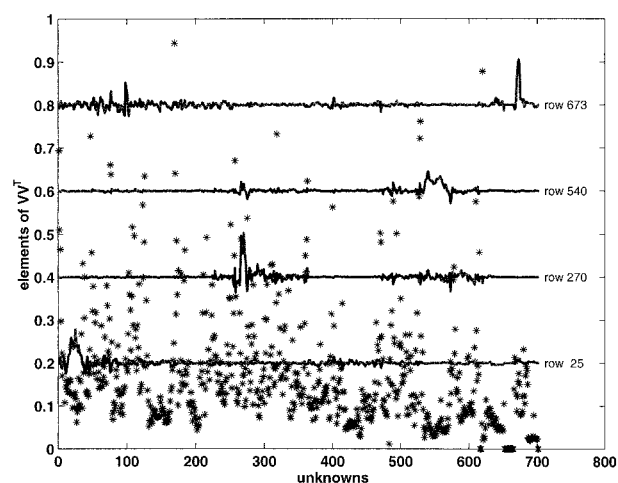


FIG. 14. The diagonal elements of the solution resolution matrix VV^T and some selected rows (row 25, 270, 540, and 673, see Table 12) scaled with a factor of 0.2 and shifted by +0.2, +0.4, +0.6, and +0.8, respectively.

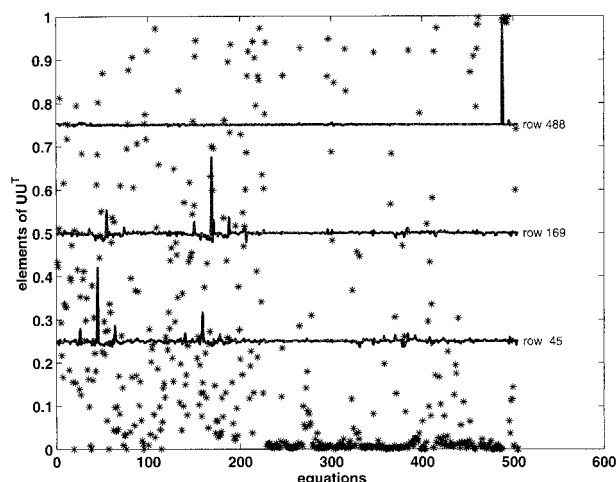


FIG. 15. The diagonal elements of the data resolution matrix UU^T and some selected rows (row 45, 169, and 488, see Table 13) scaled with a factor of 0.25 and shifted by +0.25, +0.5, and +0.75, respectively.

When comparing the obtained transports with previous estimates we have to take into account the transport associated with the net meridional mass transport. The DIC transport, for which this part of the transport is very important was discussed by Holfort et al. (1998). For the nutrient transports this part accounts for less than 10% of the total transport (see Table 6) and is therefore smaller than the errors of the inverse models (see Table 14). For the oxygen transport the contribution is about 14%. Taking into account the additional uncertainties due to wind stress and temporal variability, the effect of the meridional net mass transports is small compared to the errors. Therefore in the comparison of

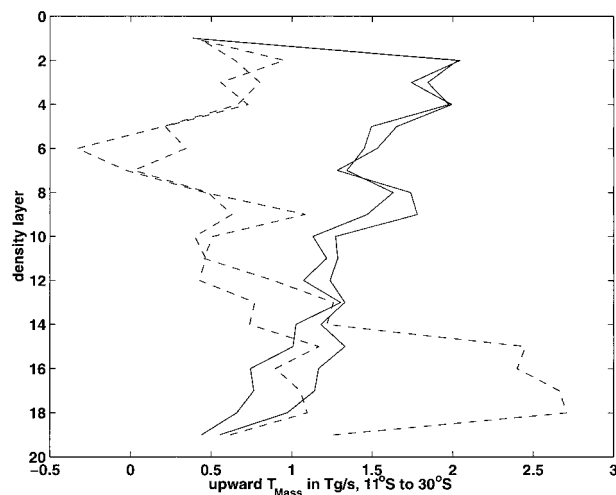


FIG. 16. The cross-isopycnal mass transport between 11°S and 30°S. Solid lines show two models where the salt conservation in the upper layer is a larger error than in the layers below. The dashed lines show two models where the assumed error in the salt conservation is assumed to be as large as in the lower layers.

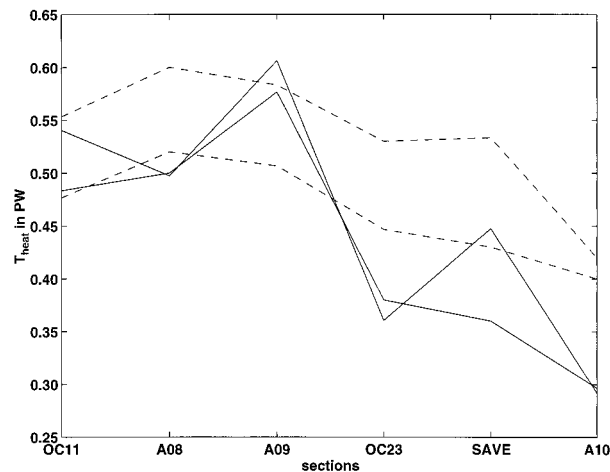


FIG. 17. Heat transport as a function of zonal section for two models with a large assumed error in the uppermost layer (solid lines) and for two models with a small error (dashed lines).

nutrient and oxygen fluxes with previous works, we do not have to take into account explicitly differences in the net mass transport.

The silica transport is generally northward, but within the error margins is indistinguishable from zero. The northward transport values decrease toward the north; this trend seems to continue in the North Atlantic (see Fig. 18b). The Atlantic between 40°S and 40°N therefore appears to be a sink for silica.

Assuming a constant Redfield ratio of $1 \mu\text{mol kg}^{-1} \text{PO}_4$ to $16 \mu\text{mol kg}^{-1} \text{NO}_3$ and taking a 4 kmol s^{-1} southward transport of PO_4 , we expect a southward NO_3 transport of 64 kmol s^{-1} . Within the error range this is also the transport we find in the inverse calculation, although the southward transport is, for all zonal sections, larger than the expected 64 kmol s^{-1} . The reasons for a larger southward NO_3 transport can be riverine input and/or a surplus of nitrogen fixation over denitrification. It is reasonable to expect a low denitrification rate in the North Atlantic because it is well ventilated and therefore has a high oxygen content. It is also known that nitrogen fixation takes place in the Sargasso Sea.

TABLE 14. Meridional transports of different properties for the zonal sections used in the analysis. Given are the mean and standard deviation of several (124 for zonal sections between 11° and 30°S, 37 for WOCE A11) inverse calculations between rank 140 and 160 with the wind stress from HR and the mean for a subset of inverse calculation with SOC climatology. Please note that heat flux is calculated for zero net meridional mass transport while a component due to net southward mass transport is included in the fluxes of other properties.

	Mass (Tg s^{-1})	Heat (PW)	Salt (Tg s^{-1})	Oxygen (kmol s^{-1})	DIC (kmol s^{-1})	NO_3 (kmol s^{-1})	PO_4 (kmol s^{-1})	SiO_4 (kmol s^{-1})	C_{anthro} (kmol s^{-1})
OCEANUS 11°S									
Mean	-1.00	0.53	-26.88	-1414	-1891	-68.2	-3.1	66	792
Std dev	0.02	0.08	0.75	297	224	25.4	1.3	99	92
SOC mean	-1.10	0.68	-26.78	-1740	-2128	-70.8	-3.3	95	833
WOCE A8 11°S									
Mean	-0.92	0.48	-26.93	-830	-2377	-94.2	-4.0	50	529
Std dev	0.03	0.09	0.58	315	162	19.5	1.0	96	95
SOC mean	-1.04	0.63	-27.52	-1110	-2682	-109.9	-4.7	59	571
WOCE A9 19°S									
Mean	-0.84	0.59	-26.30	-999	-2552	-103.8	-4.1	-18	508
Std dev	0.03	0.07	0.68	246	186	23.0	0.8	85	79
SOC mean	-0.87	0.63	-26.01	-1021	-2660	-118.7	-4.4	2	500
OCEANUS 23°S									
Mean	-0.67	0.33	-27.02	-499	-2043	-94.4	-4.1	86	334
Std dev	0.03	0.06	0.63	142	149	16.5	1.0	97	67
SOC mean	-0.69	0.36	-27.24	-593	-2061	-98.9	-4.4	119	357
SAVE 25°S									
Mean	-0.60	0.36	-26.58	-452	-1997	-66.1	-3.9	32	367
Std dev	0.04	0.06	0.60	127	162	18.7	1.1	98	73
SOC mean	-0.61	0.37	-26.46	-440	-2022	-72.2	-4.2	67	391
WOCE A10 30°S									
Mean	-0.53	0.29	-26.75	-15	-1997	-121.26	-4.2	64	317
Std dev	0.03	0.05	0.77	116	169	21.2	1.0	108	52
SOC mean	-0.54	0.28	-26.90	-31	-1959	-127.0	-4.3	102	328
WOCE A11 40°S									
Mean	-0.56	0.37	-26.37	210	-2861	-103.8	-5.9	49	245
Std dev	0.03	0.02	0.73	146	229	23.4	1.4	115	214
SOC mean	-0.60	0.35	-26.39	111	-2662	-101.5	-5.5	99	326

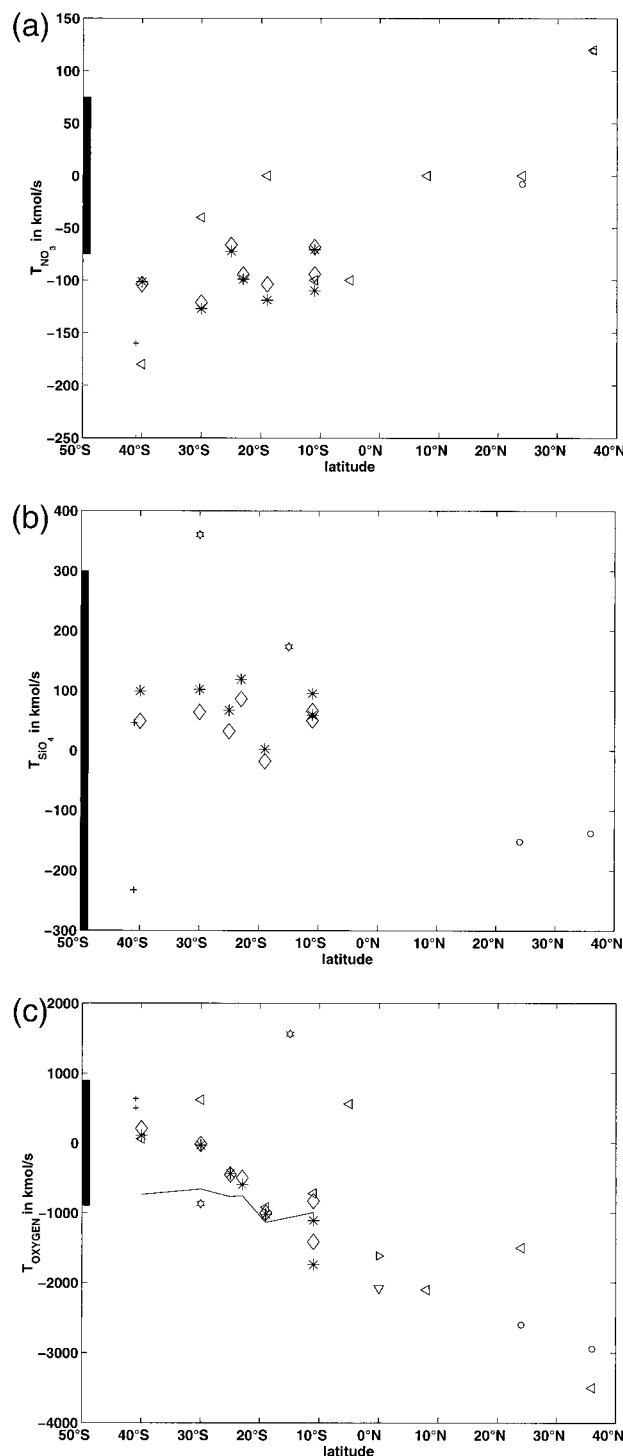


FIG. 18. The meridional transport of (a) nitrate, (b) silicate, and (c) oxygen in the Atlantic as a function of latitude. The markers denote diamonds: values with HR wind stress; stars: values with SOC wind stress; circles: Rintoul and Wunsch (1991); hexagrams: Macdonald (1993); right pointing triangle: Keeling and Peng (1995); left pointing triangle: Ganachaud and Wunsch (1998); and downward pointing triangle: Brewer et al. (1989). The bar at the left axis represents a mean error of our transports. The solid line in (c) represents the thermally driven oxygen transport (i.e., assuming 100% saturation) with HR wind stress.

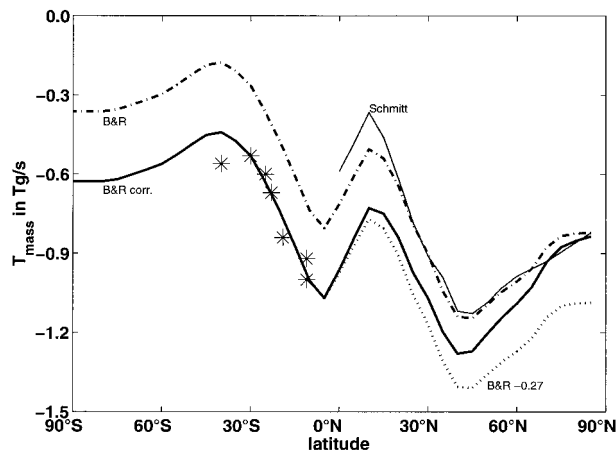


FIG. 19. Plot of T_{mass} in the Atlantic as a function of latitude calculated with HR wind stress. The dash-dotted line results from the integration of the freshwater fluxes of Baumgartner and Reichel (1975) starting at 0.8 Tg s^{-1} in the north. The dotted line is the same integration, but starting at our value of T_{mass} at 30°S , and the continuous line *corrects* the dotted line north of 11°S to arrive at 0.8 Tg s^{-1} in the north. The thin solid line represents the indirect estimate of Schmitt et al. (1989).

So a net NO_3 input into the Atlantic north of 11°S seems reasonable.

The oxygen transport between 10°S and 20°S equals the thermally driven oxygen transport, which is calculated assuming 100% oxygen saturation throughout the water column. This means that the biological pump has no effect on the net oxygen transport at these latitudes. Farther south toward 40°S the southward oxygen transport is smaller than the thermally driven oxygen transport, indicating more oxygen consumption in the southward flowing NADW than in the northward flowing waters.

Compared to our earlier heat flux estimates based on the initial LNMs, the values from the inverse analysis generally give smaller northward heat transports. Particularly the large difference in the heat transport of the two 11°S sections found in the LNM approach was reduced considerably. We compare the mean meridional heat flux values from our study with earlier direct calculations and with estimates from air-sea fluxes (Fig. 20). Although error estimates were given by some earlier authors, no error bars were attached here to the older values. An error analysis similar to the present one for the older datasets would certainly yield larger errors when considering the coarser resolution and effects of temporal variability and wind stress uncertainties. The air-sea fluxes [Bunker (1988) and SOC] were transformed into T_{heat} values, with the integration starting at the T_{heat} from our analysis at 30°S . The SOC fluxes had to be corrected with a constant offset of -30 W m^{-2} to achieve nearly zero net heat flux over the whole domain 70°S – 70°N of the SOC data. Our values are within the wide range of the previous direct estimates and, except for the 19°S value, follow closely the indirect

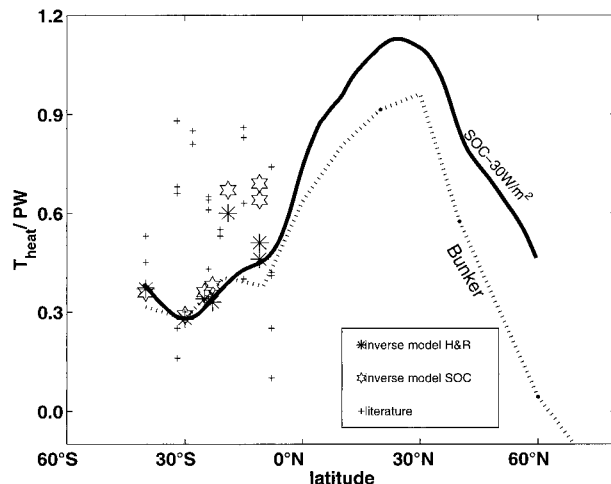


FIG. 20. Plot of T_{heat} in the Atlantic as a function of latitude. Solid stars represent values calculated with Hellermann and Rosenstein (1983) wind stress, open stars those with SOC wind stress data, crosses are previous estimates from the literature (Bryan 1962; Bennett 1978; Fu 1981; Roemmich 1983; Rintoul 1991; Macdonald 1993; Saunders and King 1995). Starting from our value at 30°S the broken line gives the heat transport from the integrated surface heat fluxes of Bunker (1988) and the continuous line the heat transport calculated with the SOC fluxes corrected for a global imbalance of 30 W m^{-2} .

estimates. The meridional distribution of T_{heat} calculated with the HR winds corresponds better to the indirect estimates than the results with SOC winds.

The high value at 19°S would imply an excessive heat gain of about 135 W m^{-2} between 23° and 19°S and a strong heat loss between 19° and 11°S. Using the SOC winds the heat convergence between 19° and 11°S almost vanishes, but the heat divergence between 19° and 23°S gets even larger. One possibility to explain this result is the assumption that a part of the Brazil Current that flows over the rather wide shelf at 19°S is missed. Because the water on the shelf is warm and salty, this flow would lower the heat transport and increase the net mass transport at 19°S. A larger T_{mass} at 19°S is also more favorable in comparison to results from an indirect method.

Similar to the indirect method of determining T_{heat} , the freshwater transport in the ocean, essentially the net mass transport, can be calculated by integrating the run-off and precipitation — evaporation (see Wijffels et al. 1992). Starting with 0.8 Sv flow from Bering Strait and integrating the combined Arctic and Atlantic freshwater fluxes of Baumgartner and Reichel (1975), the indirect method gives a value at 30°S, which is higher by 0.27 Tg s^{-1} than our direct estimate (Fig. 19), but the divergence between 30° and 11°S corresponds well to the surface fluxes. This could imply that the Baumgartner and Reichel dataset has too low precipitation values somewhere north of 11°S. The indirect estimate of Schmitt et al. (1989) of -0.8 Sv (Bering Strait) + $0.22 \text{ Sv} = -0.58 \text{ Sv}$ at the equator is even higher than the Baumgartner and Reichel estimate of $-0.8 \text{ Sv} + 0.1$

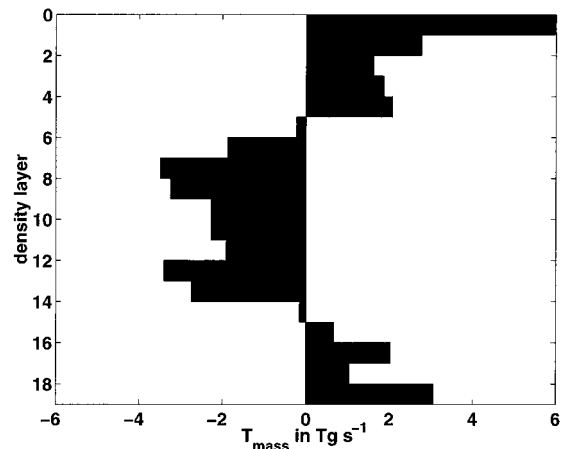


FIG. 21. Mass transport of the layers used in the inverse calculation at 30°S (see Table 2) from the model given in Table 13. Positive values represent northward flow.

$\text{Sv} = -0.7 \text{ Sv}$. The large difference at the A11 section may arise because the section is not purely zonal or because an open boundary exists in the east just south of Cape Agulhas. The Atlantic north of 11°S has a surplus of freshwater in our results.

The heat transport and/or the meridional overturning cell in the South Atlantic is often used to differentiate between the cold water path and the warm water path of the global conveyor. The meridional overturning cell (Fig. 21), has a larger net mass transport in the *warm* surface layers (about 9 Tg s^{-1}) than in the *cold* AAIW layers (about 6 Tg s^{-1}). These transport values are similar to the values of Saunders and King (1995) of approximately 10 Sv and 5 Sv , respectively, but quite different from the values of Schlitzer (1996) of 2 Sv and 11.9 Sv , respectively. The surface water transport lies within the range of estimates for the exchange of water between the Indian and Atlantic Ocean [e.g., 15 Sv by Gordon (1985); 5 Sv by Byrne et al. (1995)]. Based on their higher heat transport number at A11 Saunders and King concluded that the warm water path (Gordon 1986) of the global thermohaline circulation is the main return pathway for the southward flowing NADW. Boddem and Schlitzer (1995) obtained a lower heat transport at 30°S and concluded that the cold water path (Rintoul 1991) is more important. Our heat transport value at the A11 section at nominally 40°S is lower than the value of Saunders and King (1995) (remember, however, that the present inverse model may not be optimal for the latitude range between 30° and 45°S) and higher at 30°S than the value of Boddem and Schlitzer (1995). Following the line of arguments of earlier authors, our results lead to the conclusion that both pathways play a role, although with the warm water route being somewhat more important.

Acknowledgments. This study is a WOCE contribution. The cooperation of the *METEOR's* captain and

crew in performing the ship observations and the assistance of the staff of the Department of Marine Physics of the Institut für Meereskunde at Kiel University in the observations and the data processing was much appreciated. The study was supported by the German Ministry of Science and Technology (BMBF, Fkz:03F0121A, 03F0050D, 03F0157A).

REFERENCES

- Baumgartner, A., and E. Reichel, 1975: *Die Weltwasserbilanz*. Oldenburg Verlag, 179 pp.
- Bennet, A. F., 1978: Poleward heat fluxes in Southern Hemisphere oceans. *J. Phys. Oceanogr.*, **8**, 785–798.
- Boddem, J., and R. Schlitzer, 1995: Inter-ocean exchange and meridional mass and heat fluxes in the South Atlantic. *J. Geophys. Res.*, **100**, 15 821–15 834.
- Boebel, O., C. Schmid, and W. Zenk, 1997: Flow and recirculation of Antarctic Intermediate Water across the Rio Grande Rise. *J. Geophys. Res.*, **102**, 20 967–20 986.
- Böning, C. W., 1992: Transportprozesse im subtropischen Nordatlantik: Untersuchungen mit wirbelaflösenden Modellen der windgetriebenen und thermohalinen Zirkulation. Postdoctoral thesis, University of Kiel, 173 pp.
- Brewer, P. G., C. Goyet, and D. Dryssen, 1989: Carbon dioxide transport by ocean currents at 25°N latitude in the Atlantic Ocean. *Science*, **246**, 477–479.
- Bryan, K., 1962: Measurements of meridional heat transport by ocean currents. *J. Geophys. Res.*, **67**, 3403–3414.
- Bunker, A. F., 1988: Surface energy fluxes of the South Atlantic Ocean. *Mon. Wea. Rev.*, **116**, 809–823.
- Byrne, D. A., A. L. Gordon, and W. F. Haxby, 1995: Agulhas eddies: A synoptic view using Geosat ERM data. *J. Phys. Oceanogr.*, **25**, 902–917.
- Coachman, L. K., and K. Aagaard, 1988: Transports through Bering Strait: Annual and interannual variability. *J. Geophys. Res.*, **83**, 15 535–15 539.
- Fu, L., 1981: The general circulation and meridional heat transport of the subtropical South Atlantic determined by inverse methods. *J. Phys. Oceanogr.*, **11**, 1171–1193.
- Ganachaud, A., and C. Wunsch, 1998: Large scale oceanic nutrient and oxygen fluxes. *Int. WOCE Newslett.*, **32**, 12–15.
- Gordon, A. L., 1985: Indian–Atlantic transfer of thermocline water at the Agulhas Retroflexion. *Science*, **227**, 1030–1033.
- , 1986: Inter-ocean exchange of thermocline water. *J. Geophys. Res.*, **91**, 5037–5046.
- Hall, M. M., and H. L. Bryden, 1982: Direct estimates and mechanisms of ocean heat transport. *Deep-Sea Res.*, **29**, 339–359.
- Hellermann, S., and M. Rosenstein, 1983: Normal monthly wind stress over the world ocean with error estimates. *J. Phys. Oceanogr.*, **13**, 1093–1104.
- Hogg, N. G., P. Biscaye, W. Gardner, and W. J. Schmitz, 1982: On the transport and modification of Antarctic Bottom Water in the Vema Channel. *J. Mar. Res.*, **40** (Suppl.), 231–263.
- , W. B. Owens, G. Siedler, and W. Zenk, 1996: Circulation in the Deep Brazil Basin. *The South Atlantic: Present and Past Circulation*, G. Wefer, W. H. Berger, G. Siedler, D. J. Webb, Eds., Springer-Verlag, 249–260.
- , G. Siedler, and W. Zenk, 1999: Circulation and variability at the southern boundary of the Brazil Basin. *J. Phys. Oceanogr.*, **29**, 145–157.
- Holfort, J., 1994: Großräumige Zirkulation und meridionale Transporte im Südatlantik. *Ber. Inst. Meereskunde Univ. Kiel*, **260**, 96pp.
- , K. M. Johnson, B. Schneider, G. Siedler, and D. W. R. Wallace, 1998: Meridional transport of dissolved inorganic carbon in the South Atlantic Ocean. *Global Biogeochem. Cycles*, **12**, 479–499.
- , M. Vanicek, and G. Siedler, 2000: What causes long-term temporal changes in the South Atlantic? *Geophys. Res. Lett.*, **27**, 1187–1190.
- Houry, S., E. Dombrowsky, P. De Mey, and J. F. Minster, 1987: Brunt–Väisälä frequency and Rossby radii in the South Atlantic. *J. Phys. Oceanogr.*, **17**, 1619–1626.
- Josey, S. A., E. C. Kent, D. Oakley, and P. K. Taylor, 1996: A new global air–sea heat and momentum flux climatology. *Int. WOCE Newslett.*, **24**, 3–5.
- Keeling, R. F., and T.-H. Peng, 1995: Transport of heat, CO₂ and O₂ by the Atlantic's thermohaline circulation. *Philos. Trans. Roy. Soc. London*, **348B**, 133–142.
- Macdonald, A. M., 1993: Property fluxes at 30°S and their implications for the Pacific–Indian Troughflow and the global heat budget. *J. Geophys. Res.*, **98**, 6851–6868.
- , 1998: The global ocean circulation: A hydrographic estimate and regional analysis. *Progress in Oceanography*, Vol. 41, Pergamon, 281–382.
- Müller, T. J., and G. Siedler, 1992: Multi-year current time series in the eastern North Atlantic Ocean. *J. Mar. Res.*, **50**, 63–98.
- Onken, R., 1994: The asymmetry of western boundary currents in the upper Atlantic Ocean. *J. Phys. Oceanogr.*, **24**, 928–948.
- Reid, J. L., 1989: On the total geostrophic circulation of the South Atlantic Ocean: Flow patterns, tracers and transports. *Progress in Oceanography*, Vol. 23, Pergamon, 149–244.
- Rintoul, S. R., 1991: South Atlantic interbasin exchange. *J. Geophys. Res.*, **96**, 2675–2692.
- , and C. Wunsch, 1991: Mass, heat, oxygen and nutrient fluxes and budget in the North Atlantic Ocean. *Deep-Sea Res.*, **38** (Suppl.), 355–377.
- Roach, A. T., K. Aagaard, C. H. Pease, S. A. Salo, T. Weingartner, V. Pavlov, and M. Kulakov, 1995: Direct measurements of transport and water properties through Bering Strait. *J. Geophys. Res.*, **100**, 18 443–18 457.
- Roemmich, D., 1983: The balance of geostrophic and Ekman transports in the tropical Atlantic Ocean. *J. Phys. Oceanogr.*, **13**, 1534–1539.
- Saunders, P. M., and B. A. King, 1995: Oceanic fluxes on the WOCE A11 section. *J. Phys. Oceanogr.*, **25**, 1942–1958.
- Schlitzer, R., 1996: Mass and heat transports in the South Atlantic derived from historical hydrographic data. *The South Atlantic: Present and Past Circulation*, G. Wefer, W. H. Berger, G. Siedler, and D. J. Webb, Eds., Springer-Verlag, 83–104.
- Schmitt, R. W., P. S. Bogden, and C. E. Dorman, 1989: Evaporation minus precipitation and density fluxes for the North Atlantic. *J. Phys. Oceanogr.*, **19**, 1208–1221.
- Siedler, G., and W. Zenk, 1992: WOCE Südatlantik 1991, Reise Nr. 15, 30 Dezember 1990–23 März 1991. METEOR-Berichte 92-1, University of Hamburg, 126 pp.
- , W. Balzer, T. J. Müller, R. Onken, M. Rhein, and W. Zenk, 1993: WOCE South Atlantic 1992, Cruise No.22, 22 September 1992–31 January 1993. METEOR-Berichte 93-5, University of Hamburg, 131 pp.
- , T. J. Müller, R. Onken, M. Arhan, H. Mercier, B. A. King, and P. M. Saunders, 1996: The zonal WOCE sections in the South Atlantic. *The South Atlantic: Present and Past Circulation*, G. Wefer, W. H. Berger, G. Siedler, and D. J. Webb, Eds., Springer-Verlag, 83–104.
- Speer, K., and W. Zenk, 1993: The flow of bottom water into the Brazil Basin. *J. Phys. Oceanogr.*, **23**, 2667–2682.
- , G. Siedler, J. Pätzold, and C. Heidland, 1992: First resolution of flow through the Hunter Channel in the South Atlantic. *Earth Planet. Sci. Lett.*, **113**, 287–292.
- , J. Holfort, T. Reynaud, and G. Siedler, 1996: South Atlantic heat transport at 11°S. *The South Atlantic: Present and Past Circulation*, G. Wefer, W. H. Berger, G. Siedler, D. J. Webb, Eds., Springer-Verlag, 105–120.
- Stramma, L., 1989: The Brazil Current transport south of 23°S. *Deep-Sea Res.*, **36**, 639–646.
- STS/ODF, 1992a: South Atlantic Ventilation Experiment (SAVE). Chemical, physical and CTD data report, legs 1, 2 and 3. SIO

- Reference No. 92-9. [Available from Scripps Institution of Oceanography, La Jolla, CA 92037.]
- , 1992b: South Atlantic Ventilation Experiment (SAVE). Chemical, physical and CTD data report, Legs 4 and 5. SIO Reference No. 92-10. [Available from Scripps Institution of Oceanography, La Jolla, CA 92037.]
- , 1992c: HYDROS leg 4. Physical, chemical and CTD data, R/V *Melville* 13 March–19 April 1989. SIO Reference No. 92-12. [Available from Scripps Institution of Oceanography, La Jolla, CA 92037.]
- Tarbell, S., R. Meyer, N. Hogg, and W. Zenk, 1994: A moored array along the southern boundary of the Brazil Basin for the Deep Basin Experiment—Report of a joint experiment 1991–1992. *Ber. Inst. Meereskunde Univ. Kiel*, **243**, 97 pp.
- van Bennekom, A. J., 1996: Silica signals in the South Atlantic. *The South Atlantic: Present and Past Circulation*. G. Wefer, W. H. Berger, G. Siedler, D. J. Webb, Eds., Springer-Verlag, 345–354.
- , and G. W. Berger, 1984: Hydrography and silica budget of the Angola Basin. *Neth. J. Sea Res.*, **17**, 149–200.
- Warren, B. A., 1999: Approximating the energy transport across oceanic sections. *J. Geophys. Res.*, **104**, 7915–7919.
- , and K. G. Speer, 1991: Deep circulation in the eastern South Atlantic Ocean. *Deep-Sea Res.*, **39**, 1273–1298.
- Wijffels, S. E., R. W. Schmidt, H. L. Bryden, and A. Stigebrandt, 1992: Transport of freshwater by the ocean. *J. Phys. Oceanogr.*, **22**, 155–162.
- Wunsch, C., 1978: The North Atlantic general circulation west of 50°W determined by inverse Methods. *Rev. Geophys. Space Phys.*, **16**, 583–620.
- Wust, G., 1932: *Das ozeanographische Beobachtungsmaterial (Serienmessungen)*. Vol. 4, *Wissenschaftliche Ergebnisse der deutschen Atlantischen Expedition "Meteor" 1925–1927*. Verlag von Walter de Gruyter, 290 pp.
- , 1996: *The Ocean Circulation Inverse Problem*. Cambridge University Press, 442 pp.
- Zenk, W., and T. J. Müller, 1995: WOCE studies in the South Atlantic, cruise no. 28, 29 March–14 June 1994. *METEOR-Berichte* 95-1, University of Hamburg, 193 pp.